Cement and Concrete Research 162 (2022) 106957

Contents lists available at ScienceDirect

Cement and Concrete Research

journal homepage: www.elsevier.com/locate/cemconres

Al uptake in calcium silicate hydrate and the effect of alkali hydroxide

Y. Yan [a,b,*], B. Ma [a,c], G.D. Miron [c], D.A. Kulik [c], K. Scrivener [b], B. Lothenbach [a,d,e]

[a] Empa, Swiss Federal Laboratories for Materials Science and Technology, Laboratory for Asphalt and Concrete, Überlandstrasse 129, 8600 Dübendorf, Switzerland
[b] EPFL STI IMX LMC, MXG 230, Station 12, CH-1015 Lausanne, Switzerland
[c] Paul Scherrer Institute, Laboratory for Waste Management, Forschungsstrasse 111, 5232 Villigen PSI, Switzerland
[d] University of Bern, Institute of Geological Sciences, Rock-Water Interaction Group, Hochschulstrasse 6, 3102 Bern, Switzerland
[e] NTNU, Department of Structural Engineering, 7491 Trondheim, Norway

ARTICLE INFO

Keywords:
C-A-S-H
Aluminium uptake
Alkali hydroxide
Thermodynamic modelling

ABSTRACT

The effect of Al and of pH on the structure of calcium silicate hydrate (C-S-H), the most important hydration product in Portland and blended cement, was studied at Ca/Si ~1.0. The presence of Al led to higher amounts of secondary phases, larger interlayer distances, longer silicate chains, higher concentrations of dissolved Al and Si, and lower Ca concentrations. The amount of secondary phases progressively decreased with increasing pH; that of strätlingite and $Al(OH)_3$ dominated at low pH, and katoite at high pH values. High pH was also associated with increased Al and Si concentrations, lowered Ca concentrations, shortened silicate chain length and higher maximum $Al/Si_{C\text{-}S\text{-}H}$ ratios. The Al uptake in C-A-S-H increased with aqueous aluminium concentration. XANES analysis showed the presence of both Al(IV) and Al(VI) in different coordination environments in C-S-H.

1. Introduction

Calcium silicate hydrate (C-S-H) is the main hydration product of Portland and blended cements, and greatly affects the durability and mechanical properties of the hydrated cement. In the presence of Al-rich supplementary cementitious materials (SCMs), C-S-H can retain more Al compared to the case of plain Portland cement [1]. The use of SCMs not only lowers the CO_2 emission [2], but may also enhance long-term mechanical properties [3,4], durability [5,6] and can help to suppress alkali silica reaction [7].

C-S-H and C-A-S-H (calcium silicate hydrate containing aluminium) have a layered structure, with calcium oxide sheets sandwiched between aluminosilicate chains in a "dreierketten" arrangement as shown in Fig. 1. Within the aluminosilicate chains, the two "pairing" silicate tetrahedra are coordinated with CaO in the main layer, while the third tetrahedron, the bridging Si site, links two pairs of silicate units. Aluminium has been assumed to substitute silicon in bridging tetrahedral sites [8–11]. The silicate chain length is influenced by the Ca/Si ratio as demonstrated in several ^{29}Si NMR studies [11–19]. Bridging silicate tetrahedra are mainly present in C-S-H with low Ca/Si and largely absent at high Ca/Si. Between the layers of CaO sheets and silicate chains an interlayer region is present, which contains water molecules, Ca^{2+}, and possible alkali ions (Na^+ and/or K^+) [11]. The assignments of bands observed by FTIR and Raman spectroscopy for C(-A)-S-H [20–22] are partially contradictory due to the overlapping of spectral bands, resonance splitting, and various factors distorting the translational symmetry of real crystals [23], as Si and Al reside in topologically similar sites within the dreierketten chain. The effect of Al on the interlayer distance of C-A-S-H has been reported in several studies [11,19,24], although no clear relation between the amount of Al in C-S-H and the interlayer distance could be established.

^{27}Al MAS NMR studies indicated that the major part of Al in C-S-H is present either tetrahedrally coordinated (mainly at low Ca/Si C-S-H) and octahedrally coordinated (at high Ca/Si), while <10 % of Al is pentahedrally coordinated [8,10,25,26]. ^{27}Al MAS NMR indicated also that tetrahedral Al can have different neighbors [27], while little difference was observed for octahedrally coordinated Al in C-A-S-H. Few Al K-edge X-ray absorption spectroscopy (XAS) studies on Al-tobermorite, C-A-S-H and cement [6,28,29] have been performed so far, although XAS could provide further insights on the local structure of Al in C-A-S-H.

Different studies have shown that at higher pH values, the Al and Si concentrations are increased, along with lower Ca concentration and shorter mean silicate chain length (MCL) in C-A-S-H [24,30–33]. Despite

* Corresponding author at: Empa, Swiss Federal Laboratories for Materials Science and Technology, Laboratory for Asphalt and Concrete, Überlandstrasse 129, 8600 Dübendorf, Switzerland.
E-mail address: yiru.yan@empa.ch (Y. Yan).

https://doi.org/10.1016/j.cemconres.2022.106957
Received 7 April 2022; Received in revised form 18 August 2022; Accepted 24 August 2022
Available online 19 September 2022

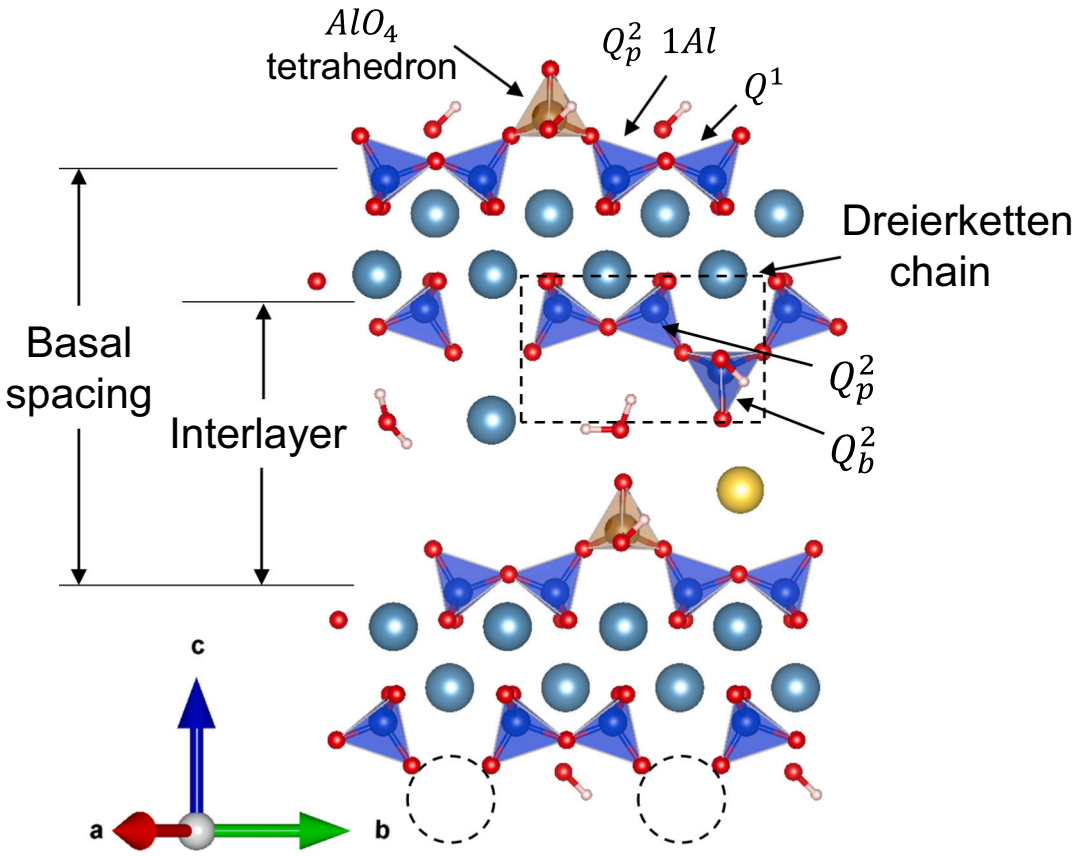

Fig. 1. Schematic structure of C-A-S-H. Spheres of blue, golden, turquoise, yellow, red and white colors represent Si, Al, Ca, Na, O and H, respectively. The dashed circles are Si tetrahedra vacancies in bridging sites. Q^n: n indicates the numbers of Si tetrahedral neighbors. Subscripts: b: bridging position, p: pairing position. (For interpretation of the references to color in this figure legend, the reader is referred to the web version of this article.)

many studies on the chemistry and structure of C(-A)-S-H [10,16,19,24,30–41], the interplay between aluminium, alkali hydroxides in solution, the structure of C-A-S-H, and the aluminium uptake by C-A-S-H is still not fully understood, as most studies focused either on the study of aqueous concentrations [32] or on the characterization of the solid phases [36,37,42]. In particular, it remains unclear whether Al or Si is preferentially taken up, and whether pH or Ca/Si would affect the uptake preferences or the coordination environment. Thus, this study is focused on the interplay between the aqueous concentrations of relevant ions, composition and structure of C-A-S-H, and the effect of alkali hydroxide on Al uptake. Experimental results are compared with the data generated by our newly developed thermodynamic model for C-S-H with aluminium and alkali, the CASH+ model [43–46]. The results and comparisons presented are important for further development of this and other thermodynamic models aimed at predicting aqueous concentrations in pore solutions of hydrated blended cements.

2. Materials and method

2.1. Synthesis procedure

SiO_2 (Aerosil 200, Evonik), CaO, $CaO{\cdot}Al_2O_3$ (CA) and NaOH/KOH solutions with concentrations of 0.1, 0.5 or 1 M at a water/solid ratio of 45 were used to synthesize C-(N,K-)A-S-H. CaO was obtained by calcining $CaCO_3$ (Merck Millipore) at 1000 °C for 12 h. CA was obtained by calcining a mixture of $CaCO_3$ and Al_2O_3 (Sigma Aldrich) in sequence at 800 °C for 1 h, at 1000 °C for 4 h and at 1400 °C for 8 h and then cooling down with a rate of 600 °C/h. The targeted molar Ca/Si ratio was $Ca/Si_{target} = 1.0$ and Al/Si ratios were $Al/Si_{target} = 0$ to 0.2. The slurry of C-(N,K-)A-S-H product was equilibrated on a shaker for 3 months and 1 year. The C-N,K-(A-)S-H samples preparation, filtration (nylon membrane, pore size 0.45 μm), washing, drying and storage at 35 % relative humidity before characterization, followed the procedure described in details by L'Hôpital et al. [19].

2.2. Analytical techniques

2.2.1. Solution analysis

The composition of the liquid phase was analyzed by ion chromatography (IC) as soon as possible after filtration in solutions diluted by factor 10, 100 and 1000 with MilliQ water to avoid any carbonation and/or precipitation. The concentrations of Ca, Na, Al and Si were quantified using a Dionex DP series ICS-3000 ionic chromatography system. Independent measurements of solutions with known compositions indicated a measurement error of ≤10 %.

The pH measurements were carried out in a non-diluted fraction of the solution with the Knick pH meter (pHMeter 766) equipped with the Knick SE100 electrode. The pH electrode was calibrated against NaOH or KOH solutions of known concentrations to minimize alkali error using the method detailed in [47]. The pH values were measured at laboratory temperature (23 to 24 °C) and corrected to 20 °C by adding +0.1 pH unit to take into account the effect of temperature on the pH measurement [30].

2.2.2. Solid phase analysis

Thermogravimetric analysis (TGA) was conducted on ground powder (~20–30 mg) under nitrogen atmosphere at a heating rate of 20 °C/min from 30 to 980 °C with a Mettler Toledo TGA/SDTA 8513 instrument. Mass losses between 30 °C and ~600 °C were assigned to dehydration and dehydroxylation of C-(N,K-)A-S-H and portlandite during

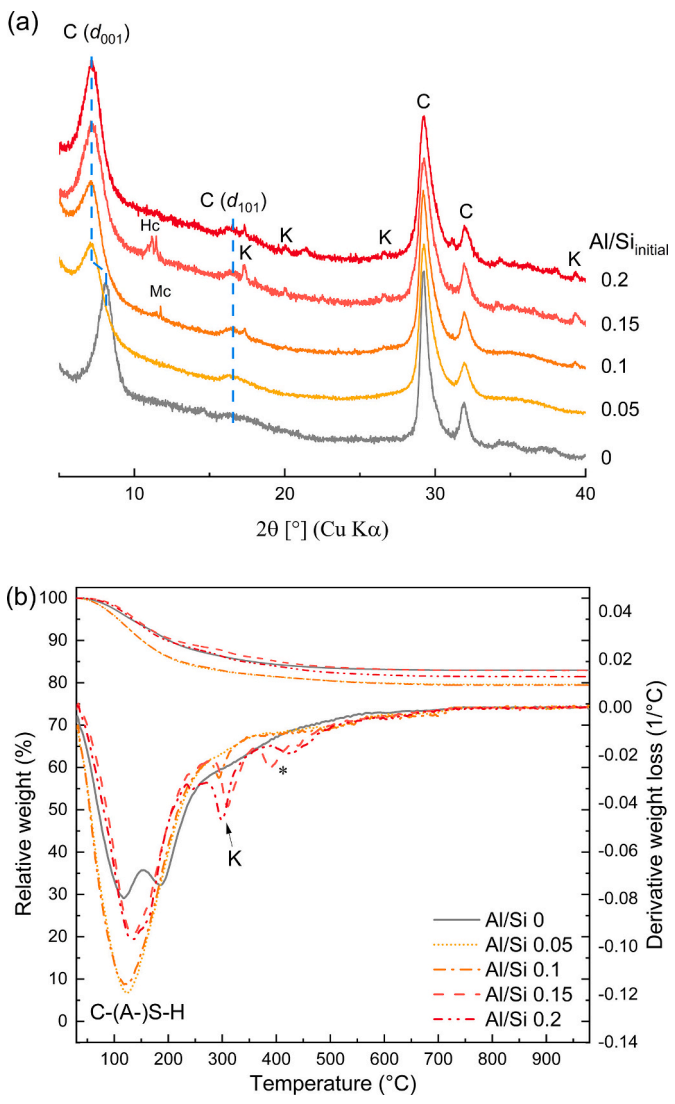

Fig. 2. XRD and TGA of C-N,K-(A-)S-H with target Ca/Si = 1.0 synthesized in NaOH 0.5 M with different initial Al/Si, equilibrated for 1 year. C: C-N,K-(A-)S-H, K: katoite ($Ca_3Al_2(OH)_6$, PDF# 00-024-0217), Hc: Hemicarbonate ($Ca_4Al_2(OH)_{12}(OH)(CO_3)_{0.5}(H_2O)_5$, PDF# 00-041-0221), Mc: monocarbonate ($Ca_4Al_2(OH)_{12}(OH)(CO_3)(H_2O)_5$, PDF# 01-087-0493). *: The weight loss between 300 and 400 °C in (b) is tentatively assigned to C-N-A-S-H.

heating. Portlandite and katoite were quantified based on the weight loss between ~350 and ~500 °C and at ~300 °C seperately using the tangential method [48] and double-checked with X-ray diffraction and Rietveld refinement analysis. Assignment of the weight loss peaks to the different hydrates was done based on the reference measurements given in [48].

Powder X-ray diffraction (XRD) data were collected using a PANalytical X'Pert Pro MPD diffractometer equipped with rotating sample stage in a θ-2θ configuration applying Cu radiation (λ = 1.54 Å) at 40 mV voltage and 40 mA, with steps of 0.019° 2θ with a fixed divergence slit size and an anti-scattering slit on the incident beam of 0.25° and 0.5° 2θ. The samples were scanned between 5° and 70° 2θ with an X'Celerator detector.

Attenuated total reflectance (ATR) Fourier Transformation Infrared (FTIR) spectra were collected by averaging 32 scans measured on a Bruker Tensor 27 FTIR spectrometer by transmittance between 340 and 4000 cm^{-1} at a resolution of 4 cm^{-1} on ~3 mg of powder. The IR spectral data obtained were preprocessed using the software package OPUS (Bruker Optics GmbH, Ettlingen, Germany). Baseline correction and normalization to the intensity of the peak at around 950 cm^{-1} were applied to every recorded spectrum. The second derivative of FTIR spectra was used in order to identify the different bands and differentiate the wavenumbers.

Raman spectra were recorded using a WITec Alpha 300 R confocal Raman microscope in backscattering geometry. A diode-pumped green laser with a wavelength of 532 nm was used in combination with a 50× objective lens. The Rayleigh scattered light was blocked by an edge filter. The backscattered light was coupled to a 300 mm lens-based spectrometer with a grating of 600 g/mm equipped with a cooled deep-depletion CCD. Back-illuminated CCD chip with 1024 × 127 pixel format, pixel size 26 × 26 μm. The laser output power was set to 20 mW. To diminish possible carbonation, the C-A-S-H powders were loaded and sealed in quartz glass capillary tubes with a 2.0 mm out diameter and 0.01 mm wall thickness. Raman spectra of the loaded and empty tubes were recorded, with the spectrum of the empty tube being subsequently subtracted. Each C-A-S-H phase was measured and averaged at 10 spots with an exposition of 10 s and 10 accumulations for each spectrum. Spectral analysis, including glass tube signal subtraction, individual baseline correction, spectra average and smoothing, was conducted using Spectragryph [49].

Aluminium K-edge (1559 eV) XANES measurements were conducted at the Phoenix II, elliptical undulator beamline at the Swiss Light Source (SLS), Paul Scherrer Institute (PSI), Villigen, Switzerland. Energy selection, X-ray energy calibration, sample preparation and measurement were followed as described in [50].

Data integration, reduction, and correction (e.g., fluorescence self-absorption) of X-ray absorption near edge structure (XANES) spectra were performed using the Demeter software package [51]. Al K-edge XANES spectra of samples were interpreted by iterative-target transformation factor analysis (ITFA) to quantify the proportions of Al-containing components [52]. FEFF8.4 [53] was employed to calculate the theoretical Al K-edge XANES spectra of representative Al coordination environments (tetrahedral AlO_4 in bridging site v.s. octahedral AlO_6 in interlayer) in C-A-S-H; the corresponding atomic structures were generated using Material Studio (MS) software V7.0.

2.2.3. C-S-H composition

The effective Ca/Si and effective Al/Si in C-S-H ($Ca/Si_{C\text{-}S\text{-}H}$ and $Al/Si_{C\text{-}S\text{-}H}$) were obtained by mass-balance calculations, considering the initial amount of CaO, CA and SiO_2 in the system, the amount of other solids present as well as the fraction of SiO_2 Al_2O_3 and CaO in solution following the procedure outlined in [30].

The amount of alkalis bound in the solid was determined following the direct method (i.e. complete acid digestion of 20 mg of washed and dried C-S-H phase in 10 mL 100 mM HCl). The total amount in the solid was obtained from the measured Ca, Na and K concentrations in the acid solution as detailed in [31]. The amount of alkali metal was also obtained indirectly from mass balance calculations using the total amount of present minus the fraction which remained in the equilibrium solution.

The incorporation of Al into C-S-H phases can also be expressed in terms of the distribution coefficient (K_d), to quantify the relative affinity for Al to sorb to C-S-H [54]. The K_d values were calculated according to:

$$K_d = \frac{C_{s,eq}}{C_{l,eq}} \approx \frac{(C_0 - C_{l,eq})}{C_{l,eq}} \times \frac{V}{M} \left(\frac{m^3}{kg}\right) \quad (1)$$

where $C_{s,eq}$ is the Al concentration sorbed into C-S-H phases [mol/kg] in equilibrium, and $C_{l,eq}$ is the aqueous concentration in equilibrium [mol/m^3]. The difference between the initial Al concentration in suspension (C_0) and the concentration determined in the supernatant ($C_{l,eq}$) corresponds to sorbed Al. M is the dry weight of the C–S–H phase [kg], and V is the volume of solution [m^3].

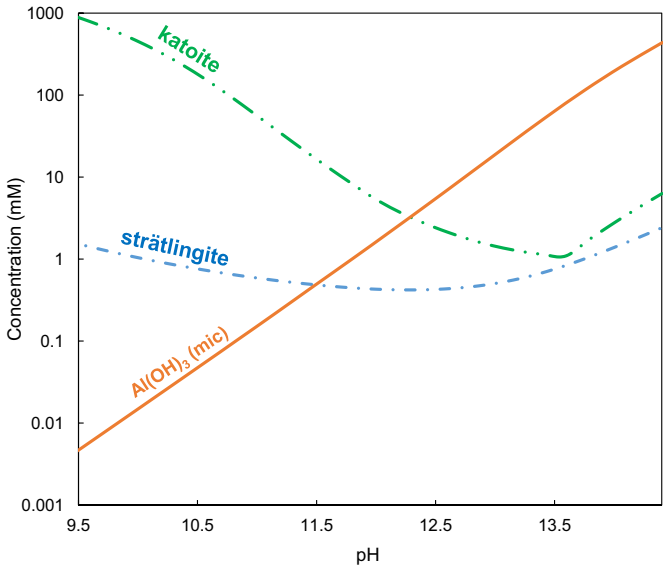

Fig. 3. Effect of pH on dissolved Al concentrations of microcrystalline $Al(OH)_3$, strätlingite and katoite (all solids 1 mol/L) at equilibrium conditions. Above pH 13.7, the formation of portlandite is calculated in the presence of katoite.

2.2.4. Thermodynamic modelling

Thermodynamic modelling was carried out with the Gibbs free energy minimization program GEM-Selektor v3.7 [55,56]. GEMS is a geochemical modelling code that computes the equilibrium speciation in aqueous, gas and stable solid phases using the Gibbs free energy minimization algorithm. The standard thermodynamic data for the species or components of aqueous, solid, and gas phases were taken from the PSI-Nagra thermodynamic database [57], while the standard molar properties for cement minerals were taken from the Cemdata18 database [58]. The C-S-H phase with alkali metal- and Al uptake was modelled using the CASH+ solid solution thermodynamic model [43–46], which has been parameterized against experimental data independent of this study. The formation of $CaSiO_2(OH)_2^0$ aquocomplex was described using log K = 4.0 for the reaction $Ca^{2+} + SiO_2(OH)_2^{2-} \Leftrightarrow CaSiO_2(OH)_2^0$ [43], instead of the log K = 4.6 reported in [57].

Saturation indices (SI) for relevant solid phases were calculated from the experimentally measured concentrations. Activity coefficients were calculated using the extended Debye-Hückel equation in Truesdell-Jones form with common ion-size parameter a_i = 3.31 Å for NaOH solutions and third parameter b_y = 0.098 kg/mol; for KOH a_i = 3.67 Å and b_y = 0.123 kg/mol [59].

3. Results and discussion

3.1. Influence of aluminium

Fig. 2 shows the effect of Al on C-S-H with Ca/Si_{target} of 1.0 in 0.5 M NaOH solution; additional data for 0.1 and 1.0 M NaOH and for 0.5 M KOH are given in the supplementary information (SI), Fig. S1. The XRD and TGA data show that C-N,K-(A-)S-H is the main phase in all cases, and indicate the formation of secondary phases at higher Al content. In 0.5 M NaOH, katoite is observed at $Al/Si_{target} \geq 0.1$, in 0.1 M NaOH already at $Al/Si_{target} \geq 0.05$ (see SI, Fig. S1), while strätlingite is observed only at 0.1 M NaOH, due to the destabilization of strätlingite with increasing pH values, as illustrated in Fig. 3. Hemicarbonate and monocarbonate are identified in some samples and their presence is attributed to minor carbonation during sample preparation, drying and measurement. Hemicarbonate can contain different amounts of carbonate [60] so the peaks can be relatively broad. A small amount of portlandite is observed only in 1 M NaOH at Al/Si_{target} = 0.15.

The TGA shows a main water loss between 30 and 300 °C from interlayer and structurally bound water in C-N,K-(A-)S-H. A hump at 400–500 °C, marked with '*', is observed at high sodium and aluminium concentrations (Al/Si_{target} = 0.15 and 0.2 in 0.5 M NaOH, Al/Si_{target} = 0.05 and 0.1 in 1 M NaOH) but not in the presence of KOH. This weight loss is tentatively assigned to thermal decomposition of more ordered water in C-N-A-S-H because none of other phases identified by TGA, XRD

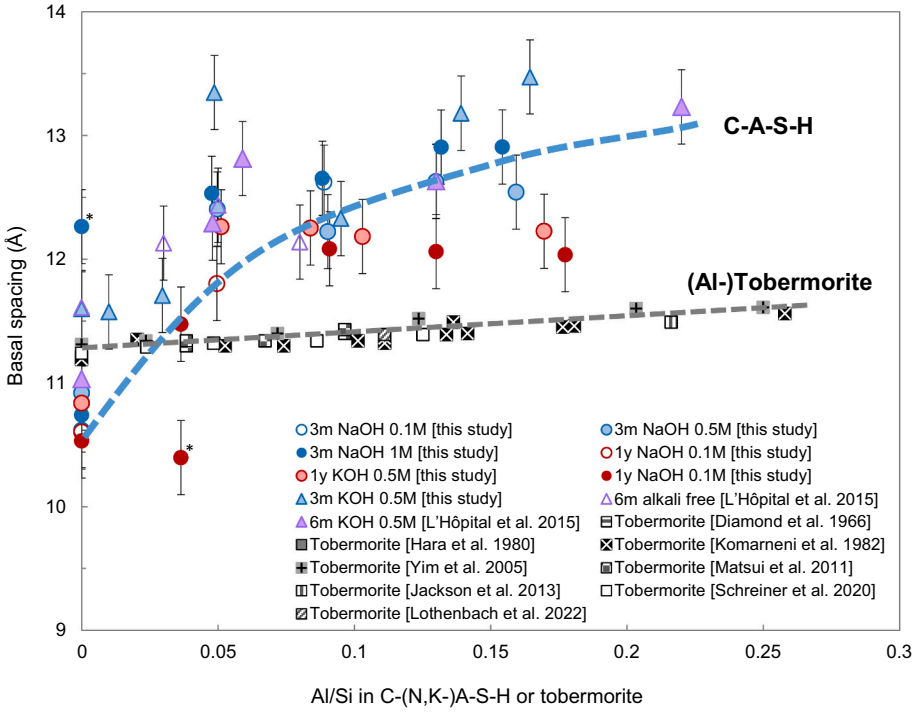

Fig. 4. Variation of the mean basal spacing as a function of Al/Si in C-(N,K-)A-S-H and (Al-)tobermorite [67,69–74]. C-A-S-H with Ca/Si_{target} at 1.0. * indicates two reflections. (For interpretation of the references to color in this figure legend, the reader is referred to the web version of this article.)

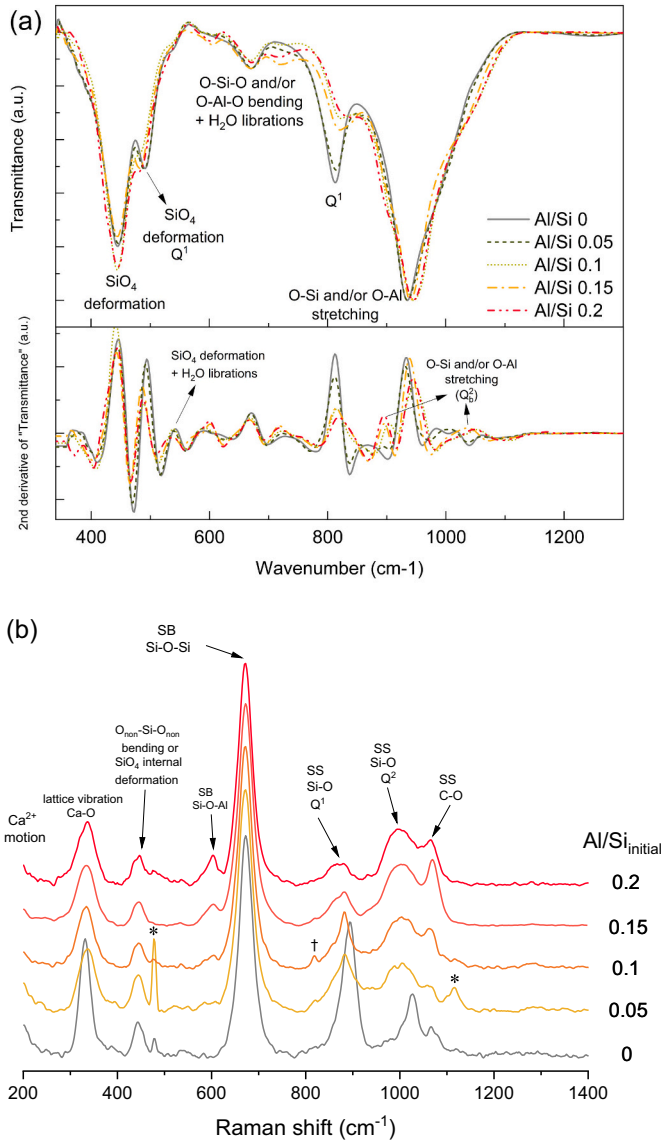

Fig. 5. (a) FTIR and second derivative and (b) Raman spectra of C-N-(A-)S-H with target Ca/Si = 1.0 after an equilibration time of 1 year with different initial Al/Si, synthesized in 0.5 M NaOH. Normalized to the most intensive band at ~970 cm^{-1} of FTIR and ~670 of Raman. *, †: unidentified peaks from secondary phases.

presented here or by Al and Si NMR [27] can explain the weight loss associated with these peaks. Similar weight losses have also been observed for C-N-A-S-H in the presence of high concentrations of NaOH [24,61] or for samples equilibrated at 50 and 80 °C [34]. TGA indicates also minor carbonation (weight loss < 0.5 %) in some samples during sample preparation, storage and/or analysis as visible in the region from 600 to 800 °C. The peaks above 800 °C are assigned to the water loss due to the decomposition of C-K-(A-)S-H to wollastonite ($CaSiO_3$) [34,62].

The position of the main C-N,K-(A-)S-H peak observed by XRD and total weight loss does not vary systematically with Al content, indicating that the presence of Al is not the primary factor controlling the interlayer and structural water content of C-N,K-(A-)S-H products. However, a broadening of the maximum diffraction at ~3.1 Å (~29° 2θ Cu Kα) is observed in the presence of Al, as shown in SI, Fig. S3. The XRD data confirm that the addition of Al leads to more secondary phases, and thus to a higher total weight loss in particular at lower NaOH and KOH concentrations. The basal spacing, d_{001}, in Fig. 2 moves to lower 2θ values in the presence of Al, indicating that the presence of aluminium

Table 1
Assignments of FTIR spectra for C-A-S-H.

FTIR absorption band (cm^{-1})	Assignment of vibration	References
400–550	Deformation of Si and/or Al tetrahedra	[75,78]
~480[a]	Deformation of Si and/or Al tetrahedral (Q^1)	[76]
~480[a]	O–Si–O and/or O–Al–O bending	[83]
~525	Si–O–Si and/or Al–O–Si bending	[83]
~525	Deformation of Si(Al) tetrahedral and water librations	[75]
670	Si–O–Si and/or Al–O–Si (O–Si–O) bending and water librations	[75,78]
810[a]	Si–O and/or Al–O stretching of Q^1 tetrahedra	[78]
920[a]	Si–O and/or Al–O stretching of Q^2 tetrahedra	[75,76]
960	Si–O and/or Al–O stretching modes	[75]
1050[a]	Si–O and/or Al–O stretching of Q^2 tetrahedra	[76]
~810, ~537	Al–O vibration from katoite	[84,85]
~536, ~670, ~954	Al–O vibration from Hc and Mc	[84]
~1360	C–O vibration from Hc and Mc	[84]
~3660	H–O vibration from katoite	[84,85]

[a] Bands visible as a shoulder.

Table 2
Assignment of Raman spectra for C-A-S-H.

Raman shift (cm^{-1})	Assignment of vibration	References
316–333	Ca–O lattice vibration	[79]
445	Internal deformation of the Si-tetrahedra	[80]
445	O–Si–O bending	[79]
477	'Breathing' vibrations of the 4-membered rings	[86,87]
~600	Si–O–Al symmetrical bending	
~670	Si–O–Si symmetrical bending	[15,79,80]
~840	Si–O symmetrical stretching Q^1	[15,79,80]
~950	Si–O symmetrical stretching Q^2	[15,79,80]
1065	C–O symmetrical stretching from hemicarboaluminate	[15]
2881, 2933, 2976	$\nu_s(CH_2)$, $\nu_s(CH_3)$, $\nu'_s(CH_3)$ from ethanol	[88]

increases the interlayer distance within C-N,K-(A-)S-H. The same effect is also observed for 0.1 and 1 M NaOH and 0.5 M KOH (see SI, Fig. S3). The broad reflection at ~17° 2θ (d-spacing ~5 Å) assigned to a d_{101} reflection indicates occupation of bridging sites in the silica chain and is more visible at higher Al/Si, which points out a prolongation of the mean silica chain length due to the incorporation of Al into the bridging sites.

The simulated Al solubility in equilibrium with amorphous $Al(OH)_3$, strätlingite and katoite with Ca/Si = 1, Al/Si = 0.1 are plotted against pH in Fig. 3. The dissolved Al concentrations of microcrystalline Al $(OH)_3$, strätlingite and katoite decrease with increasing pH, reaching minimum at pH ≈ 6.5, 12.2 and 13.6, respectively, and increase again at higher pH values, due to the increased formation of aqueous anionic aluminate species ($Al(OH)_4^-$).

Measurements of the interlayer distance in C(-A)-S-H by XRD are associated with considerable variations, as it also depends strongly on the relative humidity [63,64] and thus on the drying procedure and duration. In both, the present study and the study of L'Hôpital et al. [30], all samples were equilibrated for at least two weeks in a desiccator with the relative humidity of ~30 %, thus the water contents in C-A-S-H phases are comparable. In fact, a systematic increase of the basal spacing with Al/Si ratio in C-S-H is observed, as shown in Fig. 4. In contrast, no clear trend is found between the basal spacing and the water content (H_2O/Si obtained from TGA, see SI, Fig. S2), which confirms that the Al substitution in C-S-H is a dominant factor for the observed increase of the basal spacing.

In 0.5 M NaOH, for C-S-H without Al, a basal spacing of ~10.8 Å is

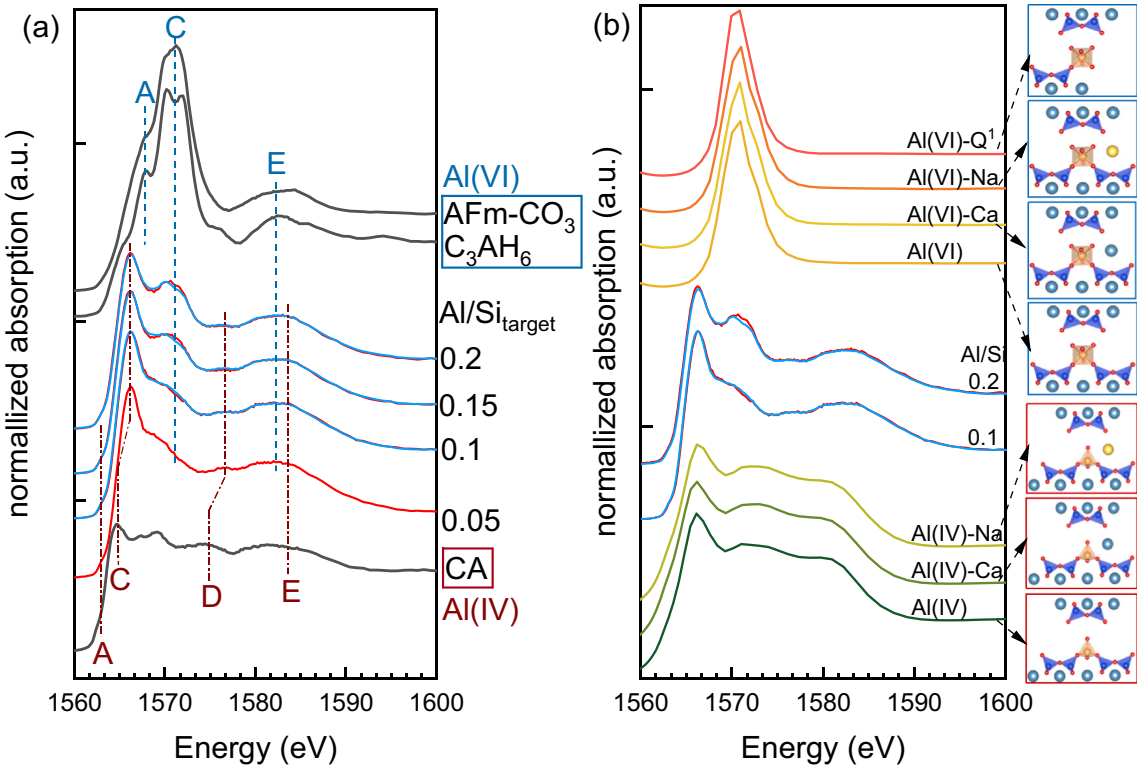

Fig. 6. (a) Al K-edge XANES spectra for C-A-S-H synthesized in NaOH 0.1 M and reference spectra for CA, C_3AH_6 and CO_3-AFm. Black and red lines: experimental spectra; blue lines: ITFA fits. (b) Comparison between selected experimental Al K-edge XANES spectra (with fitting curves in blue) and calculated spectra for tetrahedral and octahedral Al with different chemical environments. (For interpretation of the references to color in this figure legend, the reader is referred to the web version of this article.)

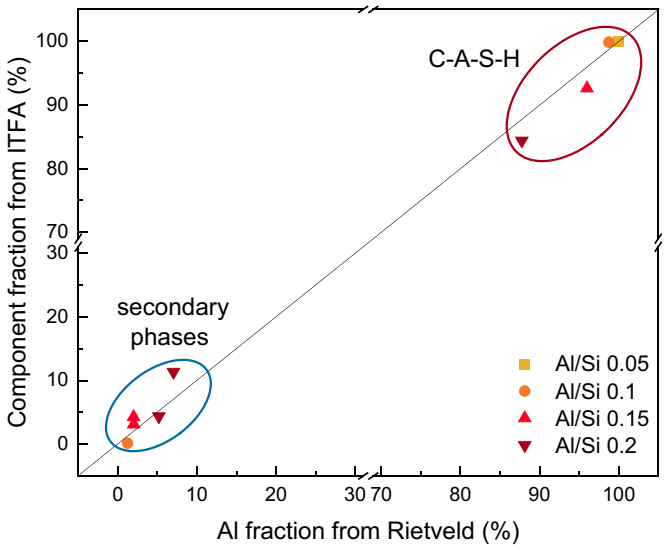

Fig. 7. Comparison between component fraction from ITFA analysis and Al fraction from Rietveld quantification.

observed, and it increases strongly to 12.3–12.5 Å at $Al/Si_{C\text{-}S\text{-}H} = 0.05$ and levels off at ~12.5 Å at higher Al contents. This broadening of the interlayer with Al can be explained i) based on the increase of negative charge due to the uptake of AlO_4 in the bridging tetrahedra, thus increasing the repulsive forces between the negatively charged main layers [19], and ii) based on the about 8–10 % longer Al–O than Si–O bonds [65,66], which is also visible in the, although more limited, increase of the interlayer distance observed for the cross-linked 11 Å Al-tobermorite [67,68] in the presence of Al, as shown in Fig. 4.

The changes in the structure upon the addition of Al have been investigated by ^{29}Si- and ^{27}Al-solid state NMR, FTIR and Raman spectroscopies, as well as by XANES. Detailed ^{29}Si- and ^{27}Al-solid state NMR investigations of these samples have recently been published by Yang et al. [27]. They show that at Ca/Si = 1.0, Al in C-S-H is mainly bound as Al(IV) in the bridging sites, with only minor amounts (<10 %) of Al(VI) present at all pH values and Al contents investigated. In addition, minor amounts of secondary phases are observed at low NaOH and/or high Al concentrations, in agreement with the XRD and TGA results reported here. The presence of Al increases the total chain length considering both Si and Al, but does not increase the length of the silica chain only [27].

Fig. 5 (a) illustrates the effect of Al on C-N-(A-)S-H deduced from the FTIR spectroscopy; the second derivative of the FTIR is also displayed as it allows to better identify partially overlapping bands. The vibrations from secondary phases are not discussed here because the maximum amount of secondary phases is <8 wt%, such that they are hidden by the bands from C-A-S-H (see Table 1). The vibrational spectra can be divided into two regions: the bands in the region 800–1200 cm^{-1} are due to stretching vibration of O–Si and/or O–Al, while from 400 cm^{-1} to 800 cm^{-1} the spectra have contributions from SiO_4 and/or AlO_4 deformation, bending vibrations of the O–Si–O and/or O–Al–O groups in the dreierketten chains and from water liberations [23,75,76], as detailed in Table 1. Fig. 5 (a) shows that the most intense band moves from 933 cm^{-1} to 947 cm^{-1} in the presence of additional Al in 0.5 M NaOH. This movement to higher wavenumbers is also observed in 0.1 M and 1 M NaOH (see SI. Figure S5). Similarly, the shoulder at ~1050 cm^{-1}, characteristic of stretching vibration of O–Si and/or O–Al in Q_b^2 position [75,76], is moving to higher wavenumbers while the bridging Q_b^2 band shifts from 920 cm^{-1} (in the absence of any Al [76]) to 880 cm^{-1} at $Al/Si_{initial} = 0.2$ (see second derivative of the FTIR in Fig. 5 (a)). This shows

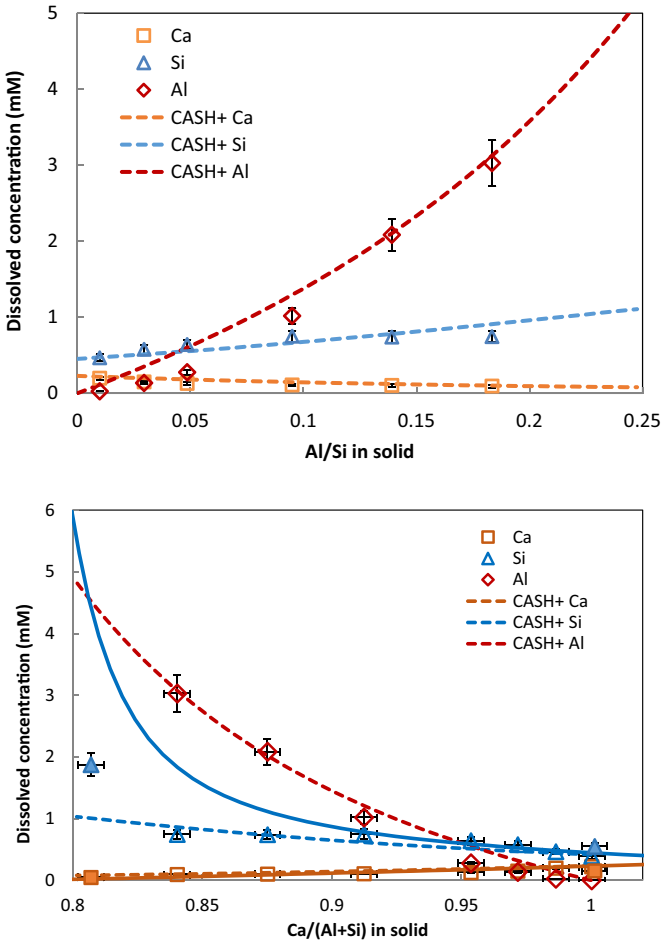

Fig. 8. Measured (symbols) and calculated (lines) concentrations of Ca, Si and Al in solutions equilibrated with target Ca/Si = 1.0 in KOH 0.5 M as a function of (a) Al/Si ratios and (b) Ca/(Al + Si). The equilibrium time is 3 months. Orange squares: Ca, blue triangles: Si and red diamonds: Al, empty ones are C-A-S-H samples and the filled ones are C-S-H samples from [76]. The estimated relative uncertainty of the IC measurements is ±10 %. Lines: modelled using the thermodynamic CASH+ solid solution model [43–46], dashed lines: simulated in C-A-S-H system, and solid lines: simulated in C-S-H system without Al. (For interpretation of the references to color in this figure legend, the reader is referred to the web version of this article.)

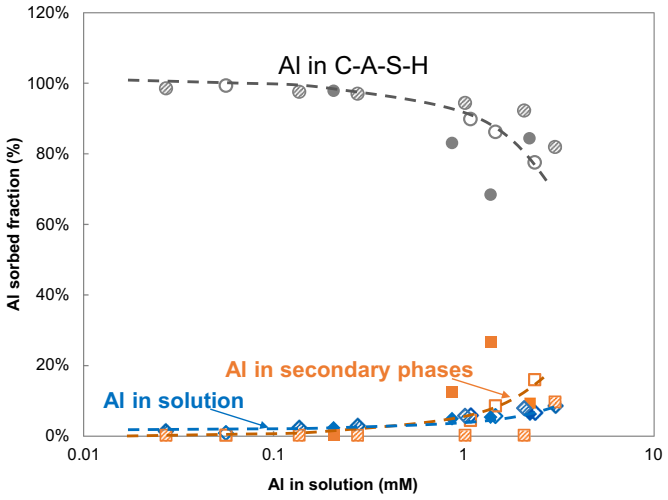

Fig. 9. Al fraction in C-A-S-H, aqueous phase and different secondary phases for target Ca/Si = 1.0 after 3 months and 1 year equilibration in the presence of 0.5 M alkali hydroxide. Empty symbols: sample synthesized for 3 months and equilibrated in 0.5 M Na OH, solid symbols: sample synthesized for 1 year and equilibrated in 0.5 M NaOH, patterned symbols: sample synthesized for 3 months and equilibrated in 0.5 M KOH. The dashed curves are eye-guide.

a higher polymerization degree of the silicate chains [77,78] due to the addition of Al, which increases the total (Al + Si)/Ca ratio. In fact, the intensity of the Q^1 signals (bands at ~810 cm^{-1} and at 490 cm^{-1}) is decreasing as more Al is present, while the Q^2_b signal at ~920 cm^{-1} increases confirming the increase of connectivity also observed by NMR [27] and the Al-uptake in the bridging sites of C-S-H.

The Raman spectra in Fig. 5 (b) show that the peak at 316–333 cm^{-1} attributing to vibrations of Ca–O [79,80] becomes weaker and broader with increasing $Al/Si_{initial}$. A peak assigned to internal deformation of the Si-tetrahedra [80] or to O–Si–O bending [79] is visible at 445 cm^{-1}, while a main Si–O–Si symmetrical bending peak is present at 670 cm^{-1}. The presence of Al had only a very weak effect on the positions of these peaks, but had a clear effect on the intensity of the signals assigned to Q^1 and Q^2 sites. The Si–O symmetrical stretching (SS) band at ~840–940 cm^{-1}, assigned to SS Q^1 [15,79,80], decreases in intensity with $Al/Si_{initial}$ indicating less Q^1. In contrast, the peak area of the signal at ~950–1040 cm^{-1}, assigned to SS Q^2 [15,79,80], increases with $Al/Si_{initial}$ confirming the FTIR data presented above and the solid state NMR [27]. The peak width of these Si–O silicate Q^1 and Q^2 signals broadens, which indicates a higher degree of disordering in the silicate chains [81,82], due to the presence of more different Q^2 species (Q^2_p, Q^2_b, and Q^2_p(1Al)) with additional Al in C-A-S-H. The peaks located at 1065 cm^{-1} are attributed to the C–O SS vibrations from hemicarboaluminate [15].

A small peak located at 602 cm^{-1} appeared at $Al/Si_{initial}$ = 0.1 and increased systematically with additional Al. Peak located at similar Raman shift has been reported for tobermorite [80] and Al-tobermorite [6,42], where it has been assigned to Q^3 or Q^3(1Al). However, in the C-A-S-H phases analyzed here, no Q^3 signal has been observed from ^{29}Si NMR [27], such that this signal is tentatively assigned to Al-O-Si symmetrical bending. A sharp peak at 477 cm^{-1} present at $Al/Si_{initial}$ = 0.05 and the peaks at 437 cm^{-1}, 1114 cm^{-1} and 2410 cm^{-1} and 810 cm^{-1} are tentatively assigned to signals from secondary phases (Table 2).

The local structure and coordination geometry of Al sites in C-A-S-H samples were further investigated by Al K-edge XANES spectra. Spectra of katoite (C_3AH_6), AFm-CO_3 (as a structural analogue to strätlingite) and $CaO{\cdot}Al_2O_3$ (CA) were collected for comparison. The Al sites in both C_3AH_6 and AFm-CO_3 are octahedrally coordinated Al(VI) with a main signal C at 1572 eV in the XANES spectra (see Fig. 6 (a)), while the main signal C of tetrahedrally coordinated Al(IV) of CA appeared at a lower energy of 1565 eV. The peaks A, C and E in Fig. 6 (a) correspond to the transitions of 1s to 3s-like, 3p-like and 3d-like states, respectively, while peak D corresponds to the multiscattering within adjacent neighbor shells [89,90]. The 1s to 3s-like transition is forbidden for the tetrahedral geometry of Al and thus results in weak peak A intensity, while it is permitted in the case of octahedral geometry due to the hybridization of s and p orbitals [89,90]. Thus, peak A is quite weak in Al(IV) predominated environments (e.g., CA and C-A-S-H), whereas it is more visible in C_3AH_6 and AFm-CO_3 where Al(VI) is predominant. The position of peak C for Al(IV) in CA is a few eV lower than the position for octahedral Al(Vl) in C_3AH_6 and AFm-CO_3, in good agreement with previous studies [29,89–93].

The iterative-target transformation factor analysis (ITFA) of the Al K-edge XANES dataset was performed to quantify the proportions of Al-containing components. XRD results suggest that the solid products mainly consist of C-A-S-H, katoite, and AFm phases. In combination with the assessments on the indicators of theoretical error functions (see SI, Table S1) and the principal component analysis (PCA), the number of abstract spectra (see SI, Fig. S7) to reproduce the Al K-edge XANES spectra of C-A-S-H samples is determined to be three. Via the iterative target test (ITT), the three components were identified as C-A-S-H, katoite, and AFm-CO_3, in good agreement with the XRD results. C-A-S-H

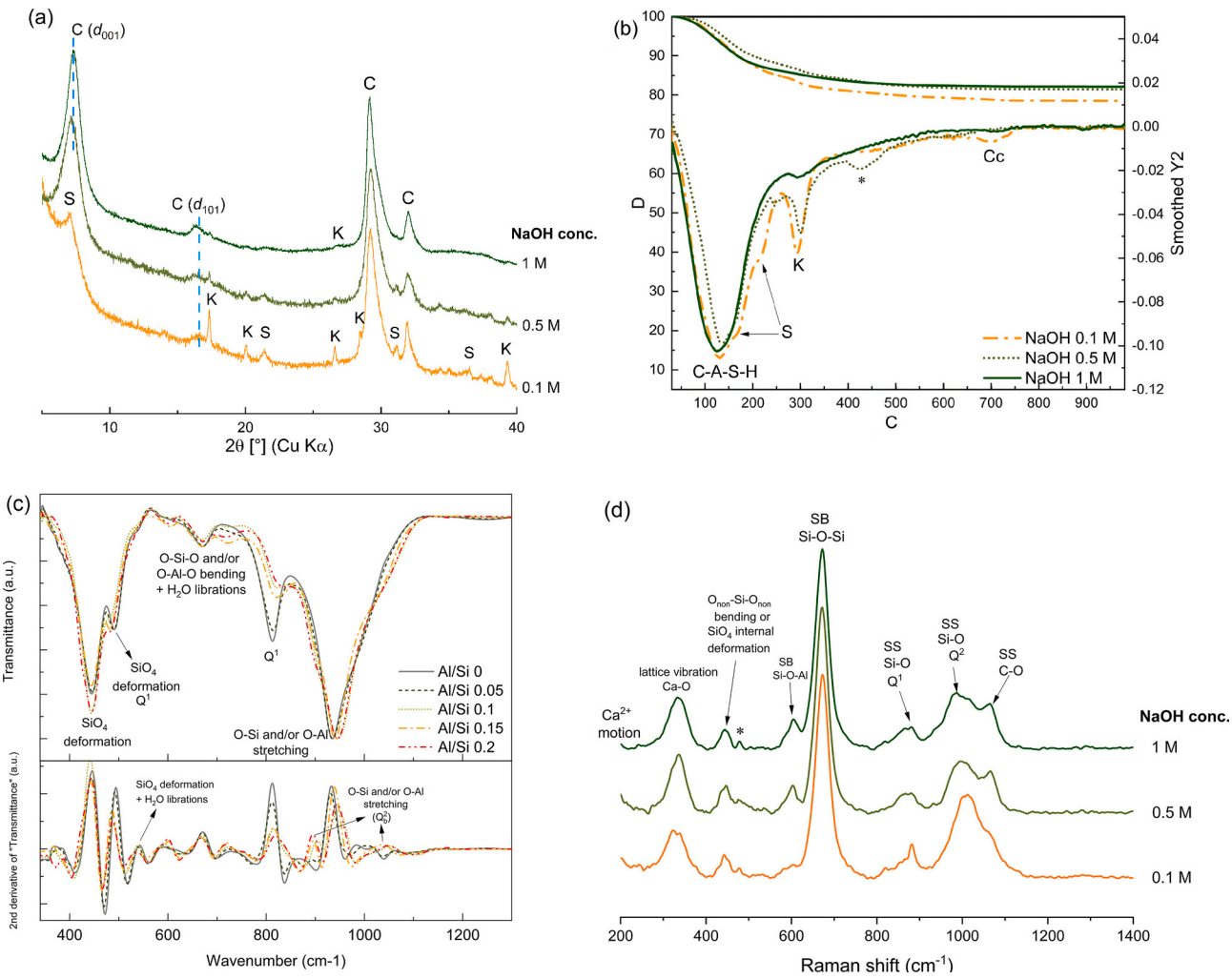

Fig. 10. (a) XRD, (b) TGA, (c) FTIR and second derivative of FTIR and (d) Raman of C-A-S-H with a target Ca/Si of 1.0 and target Al/Si of 0.2 synthesized in NaOH from 0.1 M to 1 M after an equilibrium time of 1 year. C: C-(K-)A-S-H; K: katoite, S: straetlingte, Cc: carbonates *: unidentified peak from secondary phase.

with $Al/Si_{initial} = 0.05$, having no visible secondary phases in XRD and TGA analysis, was used as a reference of pure C-A-S-H in ITFA analysis. The ITFA fitting curves together with the experimental spectra of C-A-S-H with $Al/Si_{initial}$ 0.1, 0.15, and 0.2 are illustrated in Fig. 6 (a). In accordance with XRD Rietveld analysis, ITFA analysis shows that the majority of the solid phase is C-A-S-H, and the maximum mol fraction of Al in secondary phases is about 15 %. With increasing Al/Si ratios, the intensity of peak C of C-A-S-H samples becomes stronger, partially related to the growing proportion of secondary phases such as katoite and AFm phases. A directly proportional relation can be found in the amounts of secondary phases from the quantification by ITFA and Rietveld analysis (see Fig. 7).

With increasing Al/Si ratios, the C-A-S-H sample spectra were reproduced less satisfactorily (Fig. 6 (a)), characterized by more differences compared to the fitting curves in the peak C region. It indicates some contributions from other coordination environments of Al sites not included in the ITFA fitting. The local structures of Al sites in C_3AH_6 and AFm-CO_3 are well known and not expected to change with the Al/Si ratios, which is, however, not the case for C-A-S-H. Thus, the fitting difference could result from changes of the Al coordination environment and/or Al content in C-A-S-H samples.

To further investigate the relationship between the XANES spectrum features and the local structures of Al sites in C-A-S-H, the theoretical Al K-edge XANES spectra were calculated based on the atomic structures of different possible Al-centered C-A-S-H structures, including Al(IV) in bridging site without neighboring cations, Al(IV) in bridging site with a neighboring Ca, and with a neighboring Na, loosely bound Al(VI) without neighboring cations, Al(VI) with neighboring Ca, with neighboring Na and Al(VI) at end-of-chain, Q^1, position. As shown in Fig. 6 (b), the theoretical spectra differ clearly between the coordination geometries, i.e., Al(IV) and Al(VI), in both shape and peak position. The Al (VI) spectra are characterized by a strong peak at ~1571 eV, distinct from the main peak of Al(IV) spectra at ~1566 eV. However, different second neighboring atomic shells near Al(IV) or Al(VI) have no obvious effect on the calculated spectra, which might be explained by not good enough resolution of spectrum calculation or not large enough influence of the second neighboring shell on Al K-edge XANES spectra of C-A-S-H, in particular considering that the second neighbors are light elements with little difference in mass number. The comparison between the calculated spectra and the fitted experimental spectra indicates prevailing Al(IV), which is in agreement with the Al-NMR data of these samples [27]. Note that the fitting difference is located in the same energy range as the white-line peak of Al(VI) coordination environments. Thus, the missing contribution of Al sites in ITFA should be Al(VI) sites in C-A-S-H, which would indicate that with increasing Al/Si ratios, the amount of Al(VI) sites in C-A-S-H increases or that chemical environments of Al(VI) change with the initial Al/Si.

The Al/Si ratio affects also the composition of the solutions as shown in Fig. 8, where changes of Ca, Si and Al concentrations are plotted as a function of the Al/Si in the solid. An increase of the Al/Si_{target} ratio leads

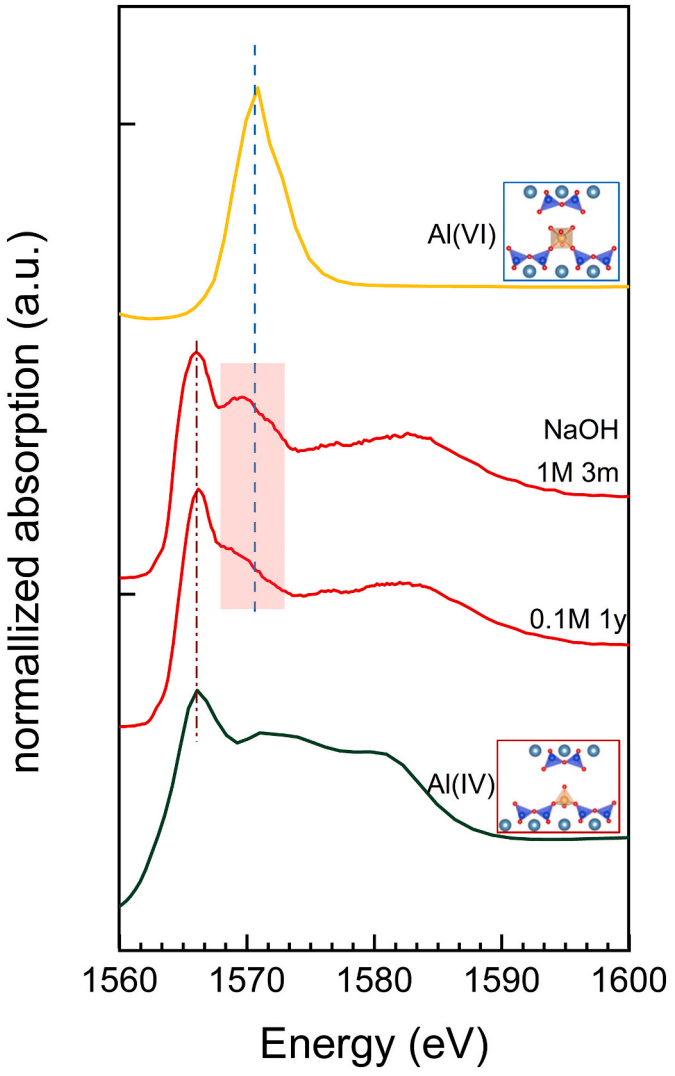

Fig. 11. K-edge XANES spectra for C-A-S-H equilibrated for 1 year in NaOH 0.1 M, C-A-S-H equilibrated for 3 months in NaOH 1 M and calculated Al(IV) and Al (VI) spectra.

to higher dissolved aluminium concentrations, while the silicon concentrations are only moderately increased indicating a lower tendency of Al than of Si to be taken up in C-A-S-H. The presence of additional aluminium also decreases the calcium concentrations. The measured dissolved concentrations are compared to the results of thermodynamic modelling using the CASH+ model [43–46] and a good agreement is observed, as shown in Fig. 8 (a).

As at $Ca/Si_{target} = 1.0$ aluminium is taken up mainly as tetrahedral Al (IV) in the "dreierketten" chains [27] (Fig. 6), the uptake of aluminium is expected to have a similar effect as the presence of more silica (Fig. 8 (b)): a higher silicon concentration and lower calcium concentration corresponding to longer silica chains due to an increase of the fraction of bridging tetrahedra. Fig. 8 (b) shows that the measured trends are much better reproduced by accounting for the effect of Al and Si separately (C-A-S-H), than if the effect of Al is considered to be the same as the effect of Si (C-S-H). While little difference is predicted at low Al contents ($Ca/(Al + Si) \geq 0.95$), a higher (Al + Si) concentration is predicted for C-A-S-H than for C-S-H, which confirms a lower tendency of Al than of Si to be in C-A-S-H at $0.81 < Ca/(Al + Si) < 0.95$.

Fig. 9 illustrates the distribution of Al between C-A-S-H, aqueous phase and different secondary phases as a function of the initial Al content. At lower Al nearly all aluminium (>99.9 %) is present in C-A-S-H. The fraction of Al bound in C-A-S-H decreases at higher Al concentrations as secondary phases precipitate for both solutions containing NaOH and KOH.

3.2. Influence of NaOH and KOH

Increasing concentrations of NaOH lower the amount of secondary as shown in Fig. 10 (a) and (b). While in 0.1 M NaOH, strätlingite and katoite are present, in 1 M NaOH, only katoite is present. Rietveld analysis indicates that the amounts of secondary phases reduce from 7 % katoite plus 5 % strätlingite in 0.1 M NaOH to 2 % katoite plus 4 % strätlingite in 0.5 M NaOH and 1 % katoite in 1 M NaOH (error ± 1 %). This is due to the destabilization of strätlingite with increasing pH values, as illustrated in Fig. 3. Fig. 10 indicates also that the presence of alkali hydroxide shows no significant influence neither on the amount of water in C-A-S-H (see main water loss up to 300 °C in TGA) nor on the basal spacing observed by XRD for C-A-S-H, see also Fig. 4. However, a somewhat more narrow d_{001} reflection is observed in 1 M NaOH compared with 0.5 M, which could indicate a more ordered structure of C-A-S-H along the *c*-axis and/or more stacking layers in *c*-axis direction [76,94]. Such a narrower d_{001} reflection has been observed previously for C-S-H without Al at higher NaOH concentrations [76], which has been assigned to an increased stacking in c-direction at higher pH values.

Fig. 10 (c) shows that increased NaOH concentrations shift the most pronounced FTIR band at 950 cm^{-1} to lower wavenumbers (redshift from 957 cm^{-1} to 943 cm^{-1}), indicating that additional NaOH depolymerizes the silicate chains [77,78], in agreement with the effect observed by Si-NMR [27] and the observations for C-S-H without Al [76]. Also the intensity of the stretching vibration of O–Si and/or O–Al from Q^1 signal located at ~810 cm^{-1} and the bending vibration of O–Si–O and/or O–Al–O [83] or the deformation of Si and/or Al tetrahedral [75,78] of Q^1 signal located at ~480 cm^{-1} increase, indicating the presence of more Q^1 silica and thus a shortening of the silica chain length. At higher NaOH concentration, the shoulders located at ~900 cm^{-1} and 1020 cm^{-1} are more visible, which indicates lowering of the symmetry resulting from the transformation of structural equivalent sites into groups of non-equivalents sites [23]. This lowering of the symmetry seems to be caused by the presence of increasing amounts of Na^+ in the interlayer, i.e. by the changes in the second coordination sphere [23].

Similar conclusions can be drawn from the Raman spectra (Fig. 10 (d)). The area of the SS Si–O Q^1 signal increases and SS Si–O Q^2 signal decreases at higher NaOH concentrations. The C-A-S-H synthesized at 1 M and 0.5 M NaOH are more prone to be carbonated than the C-A-S-H at 0.1 M NaOH. The peak at ~600 cm^{-1}, assigned to SB Si–O–Al, is more visible in C-A-S-H with 0.5 and 1 M, which indicates that increased substitution of Si by Al occurs in the presence of more alkali hydroxide. This is in agreement with the stronger uptake of Al observed by mass balance calculations (as detailed below), which was also confirmed by density function calculations, which predict a slight stabilization of Al-uptake in the presence of Na^+ [95], as well as with recent NMR observations which indicate a positive correlation between Na and Al uptake at $Ca/Si \geq 1.0$ [27].

Fig. 11 shows the Al K-edge XANES spectra of C-A-S-H with initial Al/Si 0.05 synthesized in 0.1 M NaOH for 1 year and 1 M NaOH for 3 months. These two samples were chosen to minimize the disturbance from secondary phases, since no secondary phases are visible in both samples from XRD. The energy positions of the Al(IV) peak in C-A-S-H remains the same independent of the NaOH concentration, although the peak in 0.1 M NaOH is slightly narrower. This may indicate different chemical environments of Al(IV) in C-A-S-H formed under different alkaline conditions, in agreement with recent ^{27}Al NMR data [27]. In contrast, the shape, position and intensity of the Al(VI) peaks in C-A-S-H varies and an additional signal at 1568 eV is observed, which could suggest that the content and chemical environment of octahedral Al in

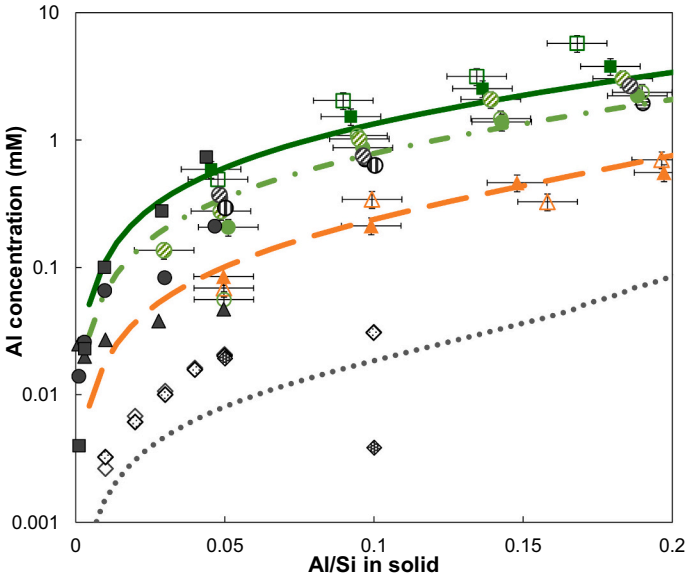

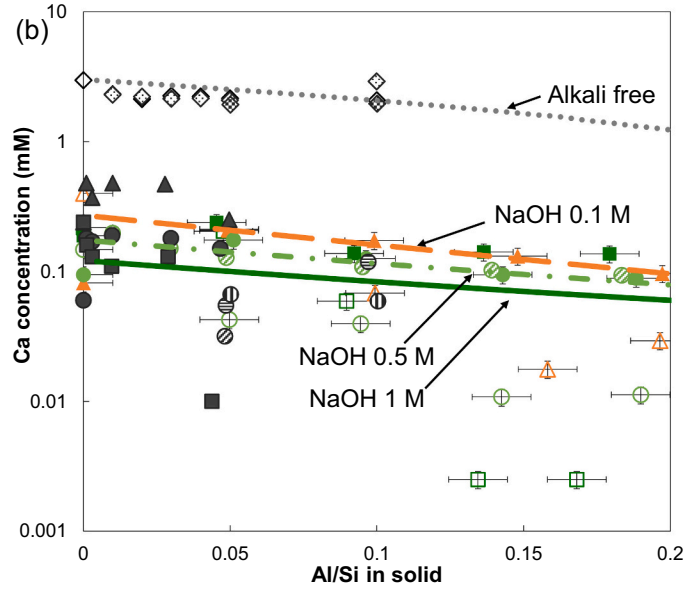

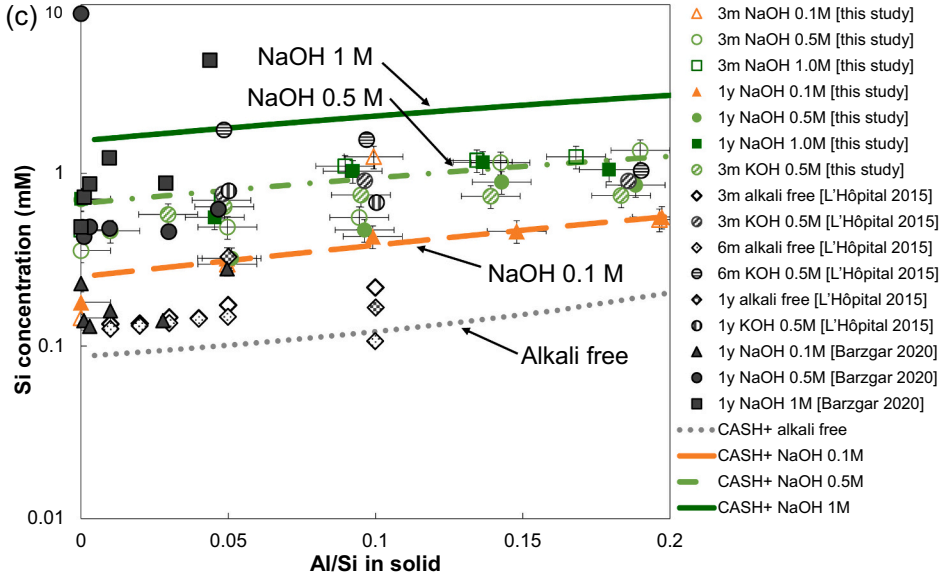

Fig. 12. Al, Si and Ca concentrations in the solutions of the C-(A-)S-H samples as a function of Al/Si ratios in solid phase. The estimated absolute errors are $\leq \pm 0.01$ units in the Al/Si ratios and the estimated relative uncertainty of the IC measurements is ±10 %. Grey symbols: C-(A)-S-H data from [30,33]; colored symbols: C-(A-)S-H from this study; diamonds: C-A-S-H in water; triangles: C-(N,K-)A-S-H with 0.1 M alkali hydroxide solution; circles: C-(N,K-)A-S-H with 0.5 M alkali hydroxide solution, squares: C-(N,K-)A-S-H with 1 M alkali hydroxide solution. Lines: simulated using the CASH+ thermodynamic solid solution model [43–46].

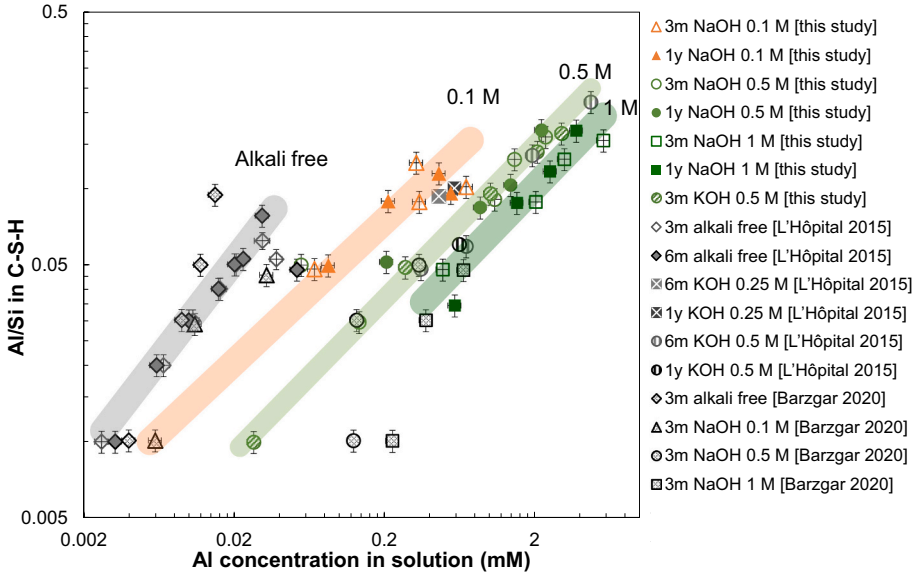

Fig. 13. Al sorption isotherms on C-A-S-H for target Ca/Si = 1.0, synthesized in different alkali hydroxides, and recorded after different equilibration times. Colored symbols: C-A-S-H from this study, grey symbols: C-A-S-H data adapted from [30,33]. (For interpretation of the references to color in this figure legend, the reader is referred to the web version of this article.)

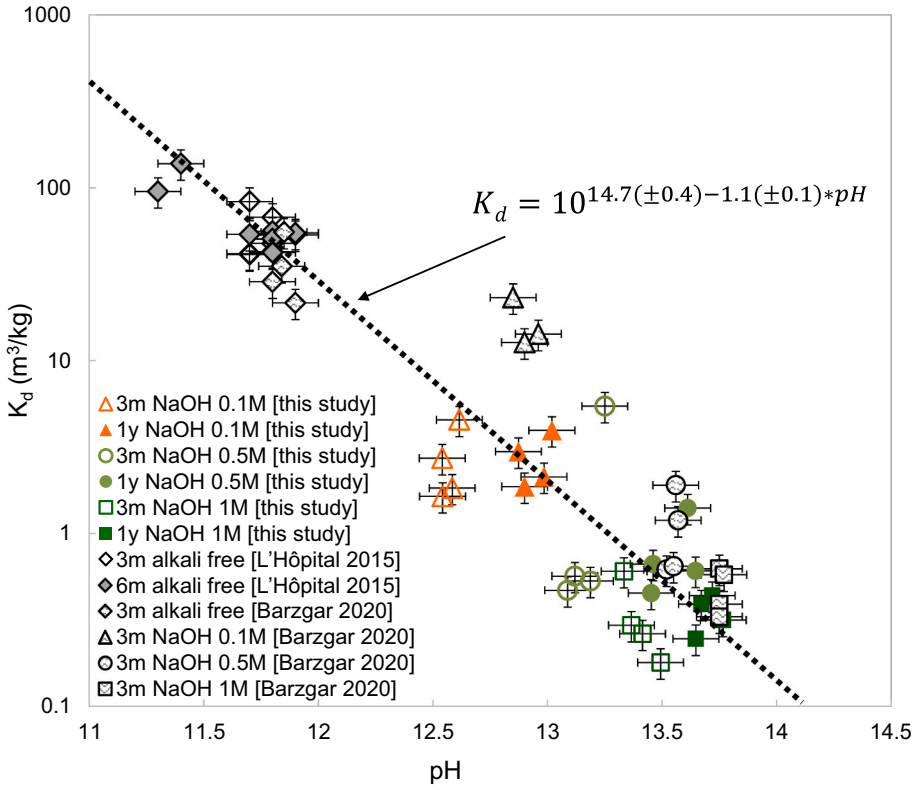

Fig. 14. Effect of pH on the K_d values of Al on C-S-H with Ca/Si = 1.

the interlayer of C-A-S-H also change with NaOH concentrations. The content of Al(VI) sites in C-A-S-H with initial Al/Si 0.05 is likely to increase or the chemical environment is different with increasing NaOH addition.

Fig. 8 showed that at constant alkali hydroxide concentration, the measured aqueous Al and Si concentrations increase with rising Al/Si_{solid}, while the Ca concentrations decrease. However, Fig. 12 illustrates the strong effect of NaOH or KOH, which further elevates aluminium and silica concentrations and lowers calcium concentrations. The concentrations measured in this study are consistent with the previous solubility data of C-A-S-H in NaOH or KOH solutions at 20 °C [30,33], although there is some scatter in the measured data points. The dissolved Al, Si and Ca concentrations show similar trends in the absence of NaOH and KOH as well as in their presence: a rise of Al and Si and a decline of Ca with increasing Al/Si_{solid}. This suggests that C-(N,K-)A-S-H solubility does not vary greatly as a function of the alkali cation (Na or

K) present, but that the concentrations are just shifted at higher pH values, due to the common ion effect with C-S-H between hydroxide, Al, Si and Ca. The measured Al, Si and Ca concentrations (data in Table A1) and their trends are in general well reproduced by thermodynamic modelling using the recent CASH+ solid solution model [43–46]. In agreement with the experimental data, the use of NaOH or KOH did not significantly affect the modelled concentrations.

The thermodynamic model predicts higher Al and Si concentrations in the presence of alkali hydroxides due to the preference of Al to form negatively charged $Al(OH)_4^-$ aqueous complexes and of Si to form $SiO(OH)_3^-$ and $SiO_2(OH)_2^{2-}$ complexes at higher pH values. The opposite effect can be observed for Ca concentration: in presence of higher concentration of alkali hydroxide, Ca concentrations decrease.

The aluminium uptake in C-S-H as a function of dissolved aluminium concentration and pH is shown in Fig. 13. The presence of alkali hydroxide increases the fraction of Al in solution and decreases the fraction in C-S-H in agreement with previous experimental studies [19,30,31,33,96], due to the increased tendency of Al to remain as $Al(OH)_4^-$ in solution at higher pH values. The maximum $Al/Si_{C\text{-}S\text{-}H}$ of C-(N, K)-A-S-H is also affected by the alkali hydroxide concentration, since at pH > 13, the Al concentrations in equilibrium with secondary phases such as katoite and strätlingite increase (see Fig. 3). The higher Al concentrations at elevated pH values allow more Al uptake in C-S-H: the maximum $Al/Si_{C\text{-}S\text{-}H}$ increases from 0.09 in alkali free solution [30] to 0.13 in 0.1 M NaOH, and to 0.17 in 1 M NaOH for C-N-A-S-H with $Al/Si_{target} = 0.2$ equilibrated for 15 months. A linear relation between aluminium concentration in aqueous solution and Al/Si in C-A-S-H at different alkali hydroxide concentrations is observed in Fig. 13.

The Al uptake in C-S-H can also be described by distribution coefficients, K_d values as defined by Eq. (1), which depict the relative affinity of Al to sorb on C-S-H, as shown in Fig. 14. While in the absence of alkali hydroxides, K_d values of 55 ± 40 m^3/kg are observed, they decrease strongly to approximately 2 in 0.1 M NaOH, to 0.6 in 0.5 M NaOH and to 0.3 in 1 M NaOH according to K_d (Ca/Si = 1.0) = $10^{14.7 (\pm 0.4) - 1.1 (\pm 0.1) * pH}$. The decrease of Al uptake at higher pH values is in accordance with ref. [33], and can be explained mainly by the fact that aluminium preferentially dissolves as $Al(OH)_4^-$ species in solution at higher pH values, which lowers the tendency of Al to be sorbed by C-S-H. The mean K_d value of ≈600 m^3/kg reported for similar C-A-S-H samples with Ca/Si = 0.8 in the absence of NaOH or KOH [97] is significantly higher, which could indicate a strong effect of pH and/or Ca/Si on the K_d values of Al on C-S-H.

4. Conclusion

In this paper we report the observed effects of Al and of KOH and NaOH concentrations on the structure and solubility of C-S-H with Ca/Si = 1.0. XRD, TGA and ITFA analysis of XANES show the presence of more secondary phases at higher Al contents and at lower pH values. The uptake of Al increases the interlayer distance of C-A-S-H, much stronger than that observed in Al-tobermorite [67], indicating that the increase of the negative charge due to the uptake of AlO_4 in the bridging tetrahedra increases the basal spacing. The uptake of Al in the bridging tetrahedral of the silica chain results in more Q^2 and less Q^1 sites as observed by FTIR and Raman spectroscopy, indicating longer dreierketten chains in C-A-S-H. In agreement with Al NMR studies [27], XANES data show that Al in C-S-H with Ca/Si = 1 is present mainly as tetrahedral Al independent of the Al concentration or pH values.

A higher initial Al loading increases both the dissolved Al and Si concentrations due to their competition for uptake in the bridging sites in the silica chain and lowers the Ca concentrations in the aqueous phase. The aqueous data show a slight preference of Si over Al for uptake in the bridging sites of C-A-S-H, although under all conditions studied, Al is predominantly bound in C-A-S-H in 0.5 M NaOH: Al in C-A-S-H > 99 % at $Al/Si_{inital} \leq 0.05$, while >70 % at $Al/Si_{initial} = 0.2$ due to the formation of secondary phases.

Higher NaOH or KOH concentrations progressively destabilize strätlingite and stabilize katoite, and reduce the amounts of secondary phases. In the C-A-S-H phase, less Q^2 and more Q^1 silicate are observed at higher pH, indicating a shortening of the silica chain length. XANES spectra show the presence of predominantly Al(IV) in the absence of alkali hydroxide, but more Al(VI) at higher pH values. High NaOH or KOH concentrations in solution also change the spectra of octahedrally bound Al(VI) but less for tetrahedral Al(IV).

At higher pH values the aqueous Al and Si concentrations increase, and Ca concentrations decrease. Higher Al concentration lead to a higher fraction of Al bound in C-A-S-H. The linear correlations between the aluminium concentration in solution and Al/Si in C-A-S-H indicate that Al is taken up at the same kind of sorption sites in C-S-H independent of Al concentration or pH values. The distribution coefficients of Al on C-S-H strongly decrease with increasing pH values.

The comparison of the measured concentrations with those predicted by thermodynamic modelling using the CASH+ solid solution model, shows in general a good agreement, thus providing an independent validation of the CASH+ model for the aluminium and alkali metals uptake in C-S-H.

CRediT authorship contribution statement

Y. Yan and B. Lothenbach conceived and designed the experiments. Y. Yan and B. Ma conducted the experiments. G. D. Miron and D. A. Kulik supported the thermodynamic modelling, K. Scrivener and B. Lothenbach supervised this work. All authors reviewed the manuscript.

Declaration of competing interest

The authors declare that they have no known competing financial interests or personal relationships that could have appeared to influence the work reported in this paper.

Data availability

Data will be made available on request.

Acknowledgement

Financial support from the Swiss National Foundation (SNF) (Project No. 200021_169014) is gratefully acknowledged. The authors would like to thank Luigi Brunetti for support to measure elemental concentration of the solution, Rico Muff and Beatrice Fischer for the help with Raman and FTIR measurements, Boris Ingold and Luigi Brunetti for the lab support. Sheng-yu Yang, Krassimir Garbev, Andreas Leemann, Ellina Bernard and Jiaqi Li are acknowledged for helpful discussions. Thomas Huthwelker and Camelia Borca (Phoenix II, SLS) are thanked for their assistance during synchrotron measurements. The synchrotron facility, SLS, is acknowledged for the allocation of beamtime (proposal number: 20182181 and 20191726).

Appendix A

Table A1
Aqueous dissolved concentrations and pH values for the C-(N,K-)A-S-H samples (target Ca/Si = 1.0).

Synthesis solution	Time (Months)	Target Al/Si	[Si] (mM)	[Ca] (mM)	[Al] (mM)	[Na] (mM)	[K] (mM)	[OH^-] (mM)	pH[a]
0.1 M NaOH	12	0	0.179	0.0818	0	82.9	0	92.7	13.0
	15	0.05	0.323	0.207	0.085	74.2	0	41.2	12.6
	15	0.1	0.431	0.173	0.212	71.0	0	38.4	12.6
	15	0.15	0.463	0.132	0.462	69.7	0	34.7	12.5
	15	0.2	0.559	0.0966	0.555	70.6	0	34.8	12.5
0.5 M NaOH	12	0	0.705	0.0945	0	473	0	322	13.5
	15	0.05	0.322	0.175	0.207	485	0	178	13.3
	15	0.1	0.470	0.126	0.869	483	0	154	13.2
	15	0.15	0.891	0.0944	1.39	468	0	132	13.1
	15	0.2	0.856	0.0889	2.22	405	0	122	13.1
1 M NaOH	12	0	0.713	0.189	0	940	0	689	13.8
	15	0.05	0.56	0.238	0.590	994	0	216	13.3
	15	0.1	1.03	0.138	1.53	974	0	232	13.4
	15	0.15	1.16	0.141	2.53	1200	0	260	13.4
	15	0.2	1.05	0.137	3.79	1027	0	312	13.5
0.1 M NaOH	3	0	0.146	0.399	0	78.7	0	111	13.0
	3	0.05	0.298	0.212	0.069	80.4	0	105	13.0
	3	0.1	1.25	0.0681	0.342	80.1	0	74.7	12.9
	3	0.15	11.4	0.0177	0.327	69.3	0	79.5	12.9
	3	0.2	0.541	0.0293	0.701	63.6	0	96.6	13.0
0.5 M NaOH	3	0	0.357	0.1476	0	472	0	341	13.5
	3	0.05	0.489	0.0426	0.056	580	0	409	13.6
	3	0.1	0.556	0.0396	1.09	493	0	289	13.5
	3	0.15	1.15	0.0108	1.47	512	0	443	13.6
	3	0.2	1.36	0.0112	2.37	511	0	284	13.5
1 M NaOH	3	0	0.472	0.218	0.00	978	0	572	13.8
	3	0.05	0.699	0.204	0.490	1097	0	524	13.7
	3	0.1	1.10	0.0591	2.04	986	0	469	13.7
	3	0.15	1.19	<0.0025	3.16	1236	0	585	13.8
	3	0.2	1.25	<0.0025	5.74	1165	0	444	13.6
0.5 M KOH	3	0	0.392	0.222	0	0	493	309	13.5
	3	0.01	0.465	0.197	0.027	0	496	309	13.5
	3	0.03	0.578	0.151	0.136	0	483	309	13.5
	3	0.05	0.641	0.128	0.276	0	503	309	13.5
	3	0.1	0.750	0.109	1.02	0	473	309	13.5
	3	0.15	0.738	0.103	2.08	0	475	297	13.5
	3	0.2	0.744	0.0936	3.03	0	478	309	13.5

[a] pH measured at ~24 °C.

Table A2
Saturation indices for the relevant reaction products in the C-A-S-H specimens: C-(A-)S-H is represents CASH+ solid solution model [43–46], portlandite: $Ca(OH)_2$, Amorphous SiO_2: SiO_2, katoite: $Ca_3Al_2(OH)_6$, strätlingite: $Ca_2Al((AlSi)_{1.11}O_2)(OH)_{12}(H_2O)_{2.25}$, AH_3 (mic): microcrystalline $Al(OH)_3$. Zeolitic phases: gismondine-P1: $Na_6Al_6Si_{10}O_{32}{\cdot}12H_2O$, natrolite: $Na_2Al_2Si_3O_{10}{\cdot}2H_2O$, zeolite X: $Na_2Al_2Si_{2.5}O_9{\cdot}6.2H_2O$.

Synthesis solution	(Months)	Target Al/Si	C-(A-)S-H	Portlandite	Amorph.-SiO_2	Katoite	Strätlingite	Gismondine-P1	Natrolite	Zeolite X	AH_3 (mic)
0.1 M NaOH	12	0	−2.5	−2.0	−4.4	–	–	–	–	–	–
	15	0.05	−0.9	−1.7	−4.1	−5.8	−2.2	−1.8	−1.4	−2.3	−2.3
	15	0.1	−0.6	−1.8	−3.9	−5.3	−1.4	−1.4	−1.0	−1.8	−1.8
	15	0.15	−0.7	−1.9	−3.9	−5.0	−1.0	−1.2	−0.8	−1.5	−1.5
	15	0.2	−0.8	−2.1	−3.8	−5.3	−1.0	−1.0	−0.6	−1.3	−1.4
0.5 M NaOH	12	0	−1.2	−1.2	−5.1	–	–	–	–	–	–
	15	0.05	−1.2	−0.9	−5.5	−4.4	−2.9	−2.5	−2.1	−2.8	−2.7
	15	0.1	−1.0	−1.1	−5.3	−3.6	−1.8	−2.0	−1.5	−2.1	−2.0
	15	0.15	−0.6	−1.2	−5.0	−3.6	−1.4	−1.6	−1.1	−1.7	−1.8
	15	0.2	−0.4	−1.3	−4.9	−3.3	−0.9	−1.4	−0.9	−1.4	−1.6
1 M NaOH	12	0	−0.7	−0.7	−5.7	–	–	–	–	–	–
	15	0.05	−0.6	−0.6	−5.9	−3.0	−2.3	−2.5	−2.0	−2.6	−2.5
	15	0.1	−0.5	−0.8	−5.6	−2.9	−1.7	−2.0	−1.5	−2.0	−2.1
	15	0.15	−0.4	−0.8	−5.7	−2.5	−1.5	−1.9	−1.4	−1.9	−2.0
	15	0.2	−0.4	−0.8	−5.6	−2.1	−1.0	−1.8	−1.3	−1.7	−1.7
0.1 M NaOH	3	0	−1.2	−1.3	−4.5	–	–	–	–	–	–
	3	0.05	−0.9	−1.6	−4.2	−5.9	−2.4	−1.9	−1.6	−2.4	−2.4
	3	0.1	−0.6	−2.2	−3.5	−6.4	−1.6	−0.8	−0.5	−1.2	−1.7
	3	0.15	−0.6	−3.6	−2.3	−10.3	−3.0	0.3	0.7	−0.1	−1.6
	3	0.2	−1.9	−2.6	−3.7	−6.7	−1.8	−0.9	−0.5	−1.2	−1.3
0.5 M NaOH	3	0	−1.3	−1.0	−5.4	–	–	–	–	–	–
	3	0.05	−2.3	−1.5	−5.4	−7.3	−5.3	−2.8	−2.4	−3.2	−3.3
	3	0.1	−1.8	−1.6	−5.2	−4.9	−2.6	−1.9	−1.4	−2.0	−2.0

(continued on next page)

Table A2 (*continued*)

Synthesis solution	(Months)	Target Al/Si	C-(A-)S-H	Portlandite	Amorph.-SiO_2	Katoite	Strätlingite	Gismondine-P1	Natrolite	Zeolite X	AH_3 (mic)
	3	0.15	−2.3	−2.1	−5.0	−6.4	−3.2	−1.5	−1.0	−1.6	−1.8
	3	0.2	−2.0	−2.1	−4.9	−5.9	−2.7	−1.3	−0.8	−1.4	−1.6
1 M NaOH	3	0	−1.0	−0.6	−5.9	–	–	–	–	–	–
	3	0.05	−0.7	−0.6	−5.8	−3.4	−2.6	−2.5	−2.0	−2.6	−2.6
	3	0.1	−1.2	−1.2	−5.6	−3.8	−2.2	−1.9	−1.4	−1.9	−2.0
	3	0.15	−16.8	−8.9	−5.8	−26.7	−17.6	−1.9	−1.4	−1.8	−1.9
	3	0.2	−16.5	−8.9	−5.7	−26.2	−17.0	−1.7	−1.2	−1.6	−1.6
0.5 M KOH	3	0	−0.9	−0.8	−5.5	–	–	–	–	–	–
	3	0.01	−0.9	−0.8	−5.4	−6.0	−4.5	−8.2	−8.4	−10.4	−3.6
	3	0.03	−0.9	−1.0	−5.3	−4.9	−3.2	−7.7	−7.8	−9.7	−2.9
	3	0.05	−0.9	−1.0	−5.3	−4.5	−2.8	−7.5	−7.6	−9.4	−2.6
	3	0.1	−0.8	−1.1	−5.1	−3.6	−1.7	−7.0	−7.1	−8.9	−2.0
	3	0.15	−0.7	−1.1	−5.2	−3.1	−1.1	−6.8	−6.9	−8.6	−1.7
	3	0.2	−0.7	−1.2	−5.2	−2.9	−0.9	−6.7	−6.8	−8.5	−1.5

Table A3
Solid phase assemblages of the C-(N,K-)A-S-H samples, as determined by XRD Rietveld analysis. The estimated absolute error is ±2 wt%.

Synthesis solution	Time	Target Al/Si	C-(N,K)-A-S-H	CH	C_3AH_6	C_2ASH_8	Hc	Mc
	(Months)		(wt%)	(wt%)	(wt%)	(wt%)	(wt%)	(wt%)
0.1 M NaOH	12	0	100					
	15	0.05	100					
	15	0.1	98.8		1.2			
	15	0.15	96.0		2.0	2.0		
	15	0.2	87.8		7.0	5.2		
0.5 M NaOH	12	0	100					
	15	0.05	100					
	15	0.1	98.4		1.1			0.4
	15	0.15	94.6		2.5		0.5	2.3
	15	0.2	98.1		2.2	3.9		
1 M NaOH	12	0	100					
	15	0.05	98.8		1.2			
	15	0.1	99.4		0.6			
	15	0.15	96.4	0.3			1.6	1.7
	15	0.2	99.0		1.0			
0.1 M NaOH	3	0	100					
	3	0.05	100					
	3	0.1	98.7		1.3			
	3	0.15	97.5	0.6	1.9			
	3	0.2	88.3		3.9	7.9		
0.5 M NaOH	3	0	100					
	3	0.05	100					
	3	0.1	99.3				0.7	
	3	0.15	98.5		1.1		0.4	
	3	0.2	96.2		1.4	2.4		
1 M NaOH	3	0	100					
	3	0.05	100					
	3	0.1	99.3	0.5			0.3	
	3	0.15	98.4	0.9			0.2	0.5
	3	0.2	97.0	0.8	0.3		0.6	1.4
0.5 M KOH	3	0	100					
	3	0.01	100					
	3	0.03	100					
	3	0.05	100					
	3	0.1	100					
	3	0.15	100					
	3	0.2	97.2		0.9			1.9

Table A4
Chemical compositions of the C-(N,K-)A-S-H products, determined from Rietveld analysis, mass balance, TGA and dissolution experiments. The estimated absolute errors are less than ±0.02 units in the Ca/Si ratios, ±0.2 units in the H_2O/Si ratios, and ±0.05 units for the 0.1 M alkali samples in the Na/Si ratios of the C-(N,K-)A-S-H products.

Synthesis solution	Time	Target Al/Si	Ca/Si	Na/Si[a]	K/Si[b]	Al/Si	H_2O/Si	Chemical formula
	(Months)							
0.1 M NaOH	12	0	1.00	0.15	0	0	1.30	$(CaO)_{1.00}(Na_2O)_{0.15}SiO_2(H_2O)_{1.3}$
	15	0.05	1.00	0.12	0	0.05	1.27	$(CaO)_{1.00}(Na_2O)_{0.12}(Al_2O_3)_{0.05}SiO_2(H_2O)_{1.3}$

(*continued on next page*)

Table A4 (*continued*)

Synthesis solution	Time (Months)	Target Al/Si	Ca/Si	Na/Si[a]	K/Si[b]	Al/Si	H_2O/Si	Chemical formula
	15	0.1	0.98	0.12	0	0.09	1.54	$(CaO)_{0.98}(Na_2O)_{0.12}(Al_2O_3)_{0.09}SiO_2(H_2O)_{1.5}$
	15	0.15	0.96	0.16	0	0.11	2.00	$(CaO)_{0.96}(Na_2O)_{0.16}(Al_2O_3)_{0.11}SiO_2(H_2O)_{2.0}$
	15	0.2	0.88	0.18	0	0.10	1.57	$(CaO)_{0.88}(Na_2O)_{0.18}(Al_2O_3)_{0.10}SiO_2(H_2O)_{1.6}$
0.5 M NaOH	12	0	1.00	0.45	0	0	1.37	$(CaO)_{1.00}(Na_2O)_{0.45}SiO_2(H_2O)_{1.4}$
	15	0.05	1.00	0.34	0	0.05	1.94	$(CaO)_{1.00}(Na_2O)_{0.34}(Al_2O_3)_{0.05}SiO_2(H_2O)_{1.9}$
	15	0.1	0.99	0.33	0	0.08	1.80	$(CaO)_{0.99}(Na_2O)_{0.33}(Al_2O_3)_{0.08}SiO_2(H_2O)_{1.8}$
	15	0.15	0.93	0.39	0	0.10	1.39	$(CaO)_{0.93}(Na_2O)_{0.39}(Al_2O_3)_{0.10}SiO_2(H_2O)_{1.4}$
	15	0.2	0.97	0.39	0	0.17	1.81	$(CaO)_{0.97}(Na_2O)_{0.39}(Al_2O_3)_{0.17}SiO_2(H_2O)_{1.8}$
1 M NaOH	12	0	1.00	0.73	0	0	1.53	$(CaO)_{1.00}(Na_2O)_{0.73}SiO_2(H_2O)_{1.5}$
	15	0.05	0.95	0.36	0	0.03	1.59	$(CaO)_{0.95}(Na_2O)_{0.36}(Al_2O_3)_{0.03}SiO_2(H_2O)_{1.6}$
	15	0.1	0.99	0.27	0	0.09	1.60	$(CaO)_{0.99}(Na_2O)_{0.27}(Al_2O_3)_{0.09}SiO_2(H_2O)_{1.6}$
	15	0.15	0.95	0.36	0	0.12	1.53	$(CaO)_{0.95}(Na_2O)_{0.36}(Al_2O_3)_{0.12}SiO_2(H_2O)_{1.5}$
	15	0.2	0.98	0.34	0	0.17	1.84	$(CaO)_{0.98}(Na_2O)_{0.34}(Al_2O_3)_{0.17}SiO_2(H_2O)_{1.8}$
0.1 M NaOH	3	0	1.00	0.09	0	0	1.14	$(CaO)_{1.00}(Na_2O)_{0.09}SiO_2(H_2O)_{1.1}$
	3	0.05	1.00	0.12	0	0.05	1.95	$(CaO)_{1.00}(Na_2O)_{0.12}(Al_2O_3)_{0.05}SiO_2(H_2O)_{1.9}$
	3	0.1	0.99	0.20	0	0.09	1.73	$(CaO)_{0.99}(Na_2O)_{0.20}(Al_2O_3)_{0.09}SiO_2(H_2O)_{1.7}$
	3	0.15	1.02	0.16	0	0.14	2.08	$(CaO)_{1.02}(Na_2O)_{0.16}(Al_2O_3)_{0.14}SiO_2(H_2O)_{2.1}$
	3	0.2	0.91	0.24	0	0.10	1.74	$(CaO)_{0.91}(Na_2O)_{0.24}(Al_2O_3)_{0.10}SiO_2(H_2O)_{1.7}$
0.5 M NaOH	3	0	1.00	0.42	0	0	1.44	$(CaO)_{1.00}(Na_2O)_{0.42}SiO_2(H_2O)_{1.4}$
	3	0.05	1.00	0.32	0	0.05	2.06	$(CaO)_{1.00}(Na_2O)_{0.32}(Al_2O_3)_{0.05}SiO_2(H_2O)_{2.1}$
	3	0.1	0.99	0.37	0	0.09	1.81	$(CaO)_{0.99}(Na_2O)_{0.37}(Al_2O_3)_{0.09}SiO_2(H_2O)_{1.8}$
	3	0.15	0.98	0.36	0	0.13	1.99	$(CaO)_{0.98}(Na_2O)_{0.36}(Al_2O_3)_{0.13}SiO_2(H_2O)_{2.0}$
	3	0.2	0.97	0.46	0	0.16	1.86	$(CaO)_{0.97}(Na_2O)_{0.46}(Al_2O_3)_{0.16}SiO_2(H_2O)_{1.9}$
1 M NaOH	3	0	1.00	0.99	0	0	2.08	$(CaO)_{1.00}(Na2O)_{0.99}SiO_2(H_2O)_{2.1}$
	3	0.05	1.00	0.45	0	0.05	1.57	$(CaO)_{1.00}(Na_2O)_{0.45}(Al_2O_3)_{0.05}SiO_2(H_2O)_{1.6}$
	3	0.1	0.99	0.34	0	0.09	1.42	$(CaO)_{0.99}(Na_2O)_{0.34}(Al_2O_3)_{0.09}SiO_2(H_2O)_{1.4}$
	3	0.15	0.97	0.38	0	0.13	1.48	$(CaO)_{0.97}(Na_2O)_{0.38}(Al_2O_3)_{0.13}SiO_2(H_2O)_{1.5}$
	3	0.2	0.95	0.52	0	0.15	1.55	$(CaO)_{0.95}(Na_2O)_{0.52}(Al_2O_3)_{0.15}SiO_2(H_2O)_{1.6}$
0.5 M KOH	3	0	1.00	0	0.11	0	1.52	$(CaO)_{1.00}(K_2O)_{0.11}SiO_2(H_2O)_{1.5}$
	3	0.01	1.00	0	0.09	0.01	1.43	$(CaO)_{1.00}(K2O)_{0.09}(Al_2O_3)_{0.01}SiO_2(H_2O)_{1.4}$
	3	0.03	1.00	0	0.16	0.03	1.44	$(CaO)_{1.00}(K_2O)_{0.16}(Al_2O_3)_{0.03}SiO_2(H_2O)_{1.4}$
	3	0.05	1.00	0	0.06	0.05	1.57	$(CaO)_{1.00}(K_2O)_{0.06}(Al_2O_3)_{0.05}SiO_2(H_2O)_{1.6}$
	3	0.1	1.00	0	0.22	0.10	1.50	$(CaO)_{1.00}(K_2O)_{0.22}(Al_2O_3)_{0.10}SiO_2(H_2O)_{1.5}$
	3	0.15	1.00	0	0.21	0.14	1.56	$(CaO)_{1.00}(K2O)_{0.21}(Al_2O_3)_{0.14}SiO_2(H_2O)_{1.6}$
	3	0.2	0.96	0	0.20	0.16	1.62	$(CaO)_{0.96}(K_2O)_{0.20}(Al_2O_3)_{0.16}SiO_2(H_2O)_{1.6}$

[a] Na/Si ratios based on direct methods [31] are associated with an error of ±0.2 units for the 0.5 M alkali samples and ±0.4 for the 1 M alkali samples.
[b] K/Si ratios based on indirect methods [31] are associated with an error of ±0.3 units.

Appendix B. Supplementary data

Supplementary data to this article can be found online at https://doi.org/10.1016/j.cemconres.2022.106957.

References

[1] F. Deschner, F. Winnefeld, B. Lothenbach, S. Seufert, P. Schwesig, S. Dittrich, F. Goetz-Neunhoeffer, J. Neubauer, Hydration of Portland cement with high replacement by siliceous fly ash, Cem. Concr. Res. 42 (2012) 1389–1400.
[2] B. Lothenbach, K. Scrivener, R.D. Hooton, Supplementary cementitious materials, Cem. Concr. Res. 41 (2011) 1244–1256.
[3] M. Ahmaruzzaman, A review on the utilization of fly ash, Prog. Energy Combust. Sci. 36 (2010) 327–363.
[4] B. Sabir, S. Wild, J. Bai, Metakaolin and calcined clays as pozzolans for concrete: a review, Cem. Concr. Compos. 23 (2001) 441–454.
[5] M.D. Jackson, S.R. Mulcahy, H. Chen, Y. Li, Q. Li, P. Cappelletti, H.R. Wenk, Phillipsite and Al-tobermorite mineral cements produced through low-temperature water-rock reactions in Roman marine concrete, Am. Mineral. 102 (2017) 1435–1450.
[6] M.D. Jackson, S.R. Chae, S.R. Mulcahy, C. Meral, R. Taylor, P. Li, A.H. Emwas, J. Moon, S. Yoon, G. Vola, H.R. Wenk, P.J.M. Monteiro, Unlocking the secrets of Al-tobermorite in Roman seawater concrete, Am. Mineral. 98 (2013) 1669–1687.
[7] Z. Shi, B. Ma, B. Lothenbach, Effect of Al on the formation and structure of alkali-silica reaction products, Cem. Concr. Res. 140 (2021), 106311.
[8] X. Pardal, F. Brunet, T. Charpentier, I. Pochard, A. Nonat, 27Al and 29Si solid-state NMR characterization of calcium-aluminosilicate-hydrate, Inorg. Chem. 51 (2012) 1827–1836.
[9] J. Skibsted, M.D. Andersen, The effect of alkali ions on the incorporation of aluminum in the calcium silicate hydrate (C-S-H) phase resulting from Portland cement hydration studied by 29Si MAS NMR, J. Am. Ceram. Soc. 96 (2013) 651–656.
[10] G.K. Sun, J.F. Young, R.J. Kirkpatrick, The role of Al in C-S-H: NMR, XRD, and compositional results for precipitated samples, Cem. Concr. Res. 36 (2006) 18–29.
[11] B. Lothenbach, A. Nonat, Calcium silicate hydrates: solid and liquid phase composition, Cem. Concr. Res. 78 (2015) 57–70.
[12] J.J. Chen, J.J. Thomas, H.F.W. Taylor, H.M. Jennings, in: Solubility and Structure of Calcium Silicate Hydrate 34, 2004, pp. 1499–1519.
[13] X. Cong, R.J. Kirkpatrick, R. James Kirkpatrick, 29Si MAS NMR study of the structure of calcium silicate hydrate, Adv. Cem. Based Mater. 3 (1996) 144–156.
[14] I.G. Richardson, The calcium silicate hydrates, Cem. Concr. Res. 38 (2008) 137–158.
[15] I.G. Richardson, J. Skibsted, L. Black, R.J. Kirkpatrick, Characterisation of cement hydrate phases by TEM, NMR and raman spectroscopy, Adv. Cem. Res. 22 (2010) 233–248.
[16] I.G. Richardson, Model structures for C-(A)-S-H(I), Acta Crystallogr. Sect. B Struct. Sci. Cryst. Eng. Mater. 70 (2014) 903–923.
[17] J. Haas, A. Nonat, From C-S-H to C-A-S-H: experimental study and thermodynamic modelling, Cem. Concr. Res. 68 (2015) 124–138.
[18] T.F. Sevelsted, J. Skibsted, Carbonation of C-S-H and C-A-S-H samples studied by 13C, 27Al and 29Si MAS NMR spectroscopy, Cem. Concr. Res. 71 (2015) 56–65.
[19] E. L'Hôpital, B. Lothenbach, D.A. Kulik, K. Scrivener, Influence of calcium to silica ratio on aluminium uptake in calcium silicate hydrate, Cem. Concr. Res. 85 (2016) 111–121.
[20] I. García-Lodeiro, A. Fernández-Jiménez, D.E. Macphee, I. Sobrados, J. Sanz, A. Palomo, Stability of synthetic calcium silicate hydrate gels in presence of alkalis, aluminum, and soluble silica, Transp. Res. Rec. J. Transp. Res. Board. 2142 (2010) 52–57.
[21] I. García Lodeiro, A. Fernández-Jimenez, A. Palomo, D.E. Macphee, Effect on fresh C-S-H gels of the simultaneous addition of alkali and aluminium, Cem. Concr. Res. 40 (2010) 27–32.
[22] E. Kapeluszna, Ł. Kotwica, A. Różycka, Ł. Gołek, Incorporation of Al in C-A-S-H gels with various Ca/Si and Al/Si ratio: microstructural and structural characteristics with DTA/TG, XRD, FTIR and TEM analysis, Constr. Build. Mater. 155 (2017) 643–653.
[23] N.V. Chukanov, Infrared Spectra of Mineral Species: Extended Library, Springer Science & Business Media, 2014.

[24] R.J. Myers, E.L. Hôpital, L. Provis, B. Lothenbach, Composition-solubility-structure relationships in calcium (alkali) aluminosilicate hydrate (C-(N, K-)A-S-H), Dalt. Trans. 44 (2015) 13530–13544.
[25] M.D. Andersen, H.J. Jakobsen, J. Skibsted, A new aluminium-hydrate species in hydrated Portland cements characterized by 27Al and 29Si MAS NMR spectroscopy, Cem. Concr. Res. 36 (2006) 3–17.
[26] G. Renaudin, J. Russias, F. Leroux, C. Cau-dit-Coumes, F. Frizon, Structural characterization of C-S-H and C-A-S-H samples-part II: local environment investigated by spectroscopic analyses, J. Solid State Chem. 182 (2009) 3320–3329.
[27] S.-Y. Yang, Y. Yan, B. Lothenbach, J. Skibsted, Sodium and tetrahedral aluminium in cementitious calcium-aluminate-silicate hydrate phases (C-A-S-H), J. Phys. Chem. C 125 (2021) 27975–27995.
[28] N. Richard, N. Lequeux, P. Boch, An X-ray absorption study of phases formed in high-alumina cements, Adv. Cem. Res. 7 (1995) 159–169.
[29] E. Wieland, R. Dähn, M. Vespa, B. Lothenbach, Micro-spectroscopic investigation of Al and S speciation in hardened cement paste, Cem. Concr. Res. 40 (2010) 885–891.
[30] E. L'Hôpital, B. Lothenbach, G. Le Saout, D. Kulik, K. Scrivener, Incorporation of aluminium in calcium-silicate-hydrates, Cem. Concr. Res. 75 (2015) 91–103.
[31] E. L'Hôpital, B. Lothenbach, K. Scrivener, D.A.A. Kulik, Alkali uptake in calcium alumina silicate hydrate (C-A-S-H), Cem. Concr. Res. 85 (2016) 122–136.
[32] S.-Y. Hong, F.P. Glasser, Alkali sorption by C-S-H and C-A-S-H gels: part II. Role of alumina, Cem. Concr. Res. 32 (2002) 1101–1111.
[33] S. Barzgar, B. Lothenbach, M. Tarik, A. Di Giacomo, C. Ludwig, The effect of sodium hydroxide on Al uptake by calcium silicate hydrates (C-S-H), J. Colloid Interface Sci. 572 (2020) 246–256.
[34] R.J. Myers, E. L'Hôpital, J.L. Provis, B. Lothenbach, Effect of temperature and aluminium on calcium (alumino)silicate hydrate chemistry under equilibrium conditions, Cem. Concr. Res. 68 (2015) 83–93.
[35] S.V. Churakov, C. Labbez, Thermodynamics and molecular mechanism of Al incorporation in calcium silicate hydrates, J. Phys. Chem. C 121 (2017) 4412–4419.
[36] G. Geng, R.J. Myers, J. Li, R. Maboudian, C. Carraro, D.A. Shapiro, P.J. M. Monteiro, Aluminum-induced dreierketten chain cross-links increase the mechanical properties of nanocrystalline calcium aluminosilicate hydrate, Sci. Rep. 7 (2017) 44032.
[37] G. Geng, R.N. Vasin, J. Li, M.J.A. Qomi, J. Yan, H.R. Wenk, P.J.M. Monteiro, Preferred orientation of calcium aluminosilicate hydrate induced by confined compression, Cem. Concr. Res. 113 (2018) 186–196.
[38] J. Li, G. Geng, R. Myers, Y.S. Yu, D. Shapiro, C. Carraro, R. Maboudian, P.J. M. Monteiro, The chemistry and structure of calcium (alumino) silicate hydrate: a study by XANES, ptychographic imaging, and wide- and small-angle scattering, Cem. Concr. Res. 115 (2019) 367–378.
[39] J. Li, W. Zhang, K. Garbev, P.J.M. Monteiro, Coordination environment of si in calcium silicate hydrates, silicate minerals, and blast furnace slags: a XANES database, Cem. Concr. Res. 143 (2021), 106376.
[40] M.D. Andersen, H.J. Jakobsen, J. Skibsted, Incorporation of aluminum in the calcium silicate hydrate (C-S-H) of hydrated Portland cements: a high-field 27Al and 29Si MAS NMR investigation, Inorg. Chem. 42 (2003) 2280–2287.
[41] G. Renaudin, J. Russias, F. Leroux, F. Frizon, C. Cau-dit-Coumes, Structural characterization of C-S-H and C-A-S-H samples-part I: long-range order investigated by rietveld analyses, J. Solid State Chem. 182 (2009) 3312–3319.
[42] J. Li, W. Zhang, K. Garbev, G. Beuchle, P.J.M. Monteiro, Influences of cross-linking and Al incorporation on the intrinsic mechanical properties of tobermorite, Cem. Concr. Res. 136 (2020), 106170.
[43] D.A. Kulik, G.D. Miron, B. Lothenbach, A structurally-consistent CASH+ sublattice solid solution model for fully hydrated C-S-H phases: thermodynamic basis, methods, and ca-si-H2O core sub-model, Cem. Concr. Res. 151 (2022), 106585.
[44] G.D. Miron, D.A. Kulik, Y. Yan, J. Tits, B. Lothenbach, Extensions of CASH+ thermodynamic solid solution model for the uptake of alkali metals and alkaline earth metals in C-S-H, Cem. Concr. Res. 152 (2022), 106667.
[45] G.D. Miron, D.A. Kulik, Y. Yan, B. Lothenbach, Extensions of CASH+ thermodynamic solid solution model for the uptake of aliminium in C-S-H, 2022 in preparation.
[46] G.D. Miron, D.A. Kulik, B. Lothenbach, Porewater composition of ordinary Portland cement with and without silica fume cal-culated using the fine-tuned CASH+NK solid solution model, Mater. Struct. (2022) accepted.
[47] B. Traynor, H. Uvegi, E. Olivetti, B. Lothenbach, R.J. Myers, Methodology for pH measurement in high alkali cementitious systems, Cem. Concr. Res. 135 (2020), 106122.
[48] B. Lothenbach, P. Durdzinski, K.De Weerdt, Thermogravimetric analysis, in: K. L. Scrivener, R. Snellings, B. Lothenbach (Eds.), A Pract. Guid. to Microstruct. Anal. Cem. Mater, CRC Press, Oxford, UK, 2016, pp. 177–212.
[49] F. Menges, Spectragryph - optical spectroscopy software, Version 1.2.15. http://www.effemm2.de/spectr, 2020.
[50] B. Ma, A. Fernandez-Martinez, A. Mancini, B. Lothenbach, Spectroscopic investigations on structural incorporation pathways of FeIII into zeolite frameworks in cement-relevant environments, Cem. Concr. Res. 140 (2021), 106304.
[51] B. Ravel, M. Newville, ATHENA, ARTEMIS, HEPHAESTUS: data analysis for X-ray absorption spectroscopy using IFEFFIT, J. Synchrotron Radiat. 12 (2005) 537–541.
[52] A. Roßberg, T. Reich, G. Bernhard, Complexation of uranium(VI) with protocatechuic acid-application of iterative transformation factor analysis to EXAFS spectroscopy, Anal. Bioanal. Chem. 376 (2003) 631–638.
[53] A.L. Ankudinov, A.I. Nesvizhskii, J.J. Rehr, Dynamic screening effects in x-ray absorption spectra, Phys. Rev. B - Condens. Matter Mater. Phys. 67 (2003) 6.
[54] D.W. Oscarson, H.B. Hume, Effect of the Solid: Liquid Ratio on the Sorption of Sr2+ and Cs+ on Bentonite, Woodhead Publishing Limited, 1998.
[55] T. Wagner, D.A. Kulik, F.F. Hingerl, S.V. Dmytrievava, Gem-selektor geochemical modeling package: TSolMod library and data interface for multicomponent phase models, Can. Mineral. 50 (2012) 1173–1195.
[56] D.A. Kulik, T. Wagner, S.V. Dmytrieva, G. Kosakowski, F.F. Hingerl, K. V. Chudnenko, U.R. Berner, GEM-selektor geochemical modeling package: revised algorithm and GEMS3K numerical kernel for coupled simulation codes, Comput. Geosci. 17 (2013) 1–24.
[57] T. Thoenen, W. Hummel, U. Berner, E. Curti, The PSI/Nagra Chemical Thermodynamic Database 12/07, 5232 Villigen PSI, 2014.
[58] B. Lothenbach, D.A. Kulik, T. Matschei, M. Balonis, L. Baquerizo, B. Dilnesa, G. D. Miron, R.J. Myers, Cemdata18: a chemical thermodynamic database for hydrated Portland cements and alkali-activated materials, Cem. Concr. Res. 115 (2019) 472–506.
[59] H.C. Helgeson, D.H. Kirkham, G.G. Flowers, Theoretical prediction of the thermodynamic behavior of aqueous electrolytes at high pressure and temperature: IV. Calculation of activity coefficients, osmotic coefficients, and apparent molal and standard and relative partial molal properties to 600°C a, Am. J. Sci. 281 (1981) 1249–1516.
[60] T. Runčevski, R.E. Dinnebier, O.V. Magdysyuk, H. Pöllmann, Crystal structures of calcium hemicarboaluminate and carbonated calcium hemicarboaluminate from synchrotron powder diffraction data, Acta Crystallogr. Sect. B Struct. Sci. 68 (2012) 493–500.
[61] S. Barzgar, M. Tarik, C. Ludwig, B. Lothenbach, The effect of equilibration time on Al uptake in C-S-H, Cem. Concr. Res. 144 (2021), 106438.
[62] E. Tajuelo Rodriguez, K. Garbev, D. Merz, L. Black, I.G. Richardson, Thermal stability of C-S-H phases and applicability of Richardson and Groves' and Richardson C-(A)-S-H(I) models to synthetic C-S-H, Cem. Concr. Res. 93 (2017) 45–56.
[63] R. Smith, P. Bayliss, Interlayer desorption of CSH(1), Cem. Concr. Res. 2 (1972) 634–646.
[64] P. Bayliss, Further interlayer desorption studies of CSH(1), Cem. Concr. Res. 3 (1973) 185–188.
[65] M.W. Barnes, B.E. Scheetz, The chemistry of Al-tobermorite and its coexisting phases at 175°C, MRS Proc. 179 (1989) 243–272.
[66] R.D. Shannon, Revised effective ionic radii and systematic studies of interatomie distances in halides and chaleogenides, Acta Crystallogr. Sect. A. A 32 (1976) 751–767.
[67] B. Lothenbach, D. Jansen, Y. Yan, J. Schreiner, Solubility and characterization of synthesized Al-tobermorite, Cem. Concr. Res. 159 (2022).
[68] J. Schreiner, F. Goetz-Neunhoeffer, J. Neubauer, D. Jansen, Hydrothermal synthesis of 11 Å tobermorite – effect of adding metakaolin to the basic compound, Appl. Clay Sci. 185 (2020).
[69] M.D. Jackson, J. Moon, E. Gotti, R. Taylor, S.R. Chae, M. Kunz, A.H. Emwas, C. Meral, P. Guttmann, P. Levitz, H.R. Wenk, P.J.M. Monteiro, Material and elastic properties of Al-tobermorite in ancient roman seawater concrete, J. Am. Ceram. Soc. 96 (2013) 2598–2606.
[70] S. Komarneni, D.M. Roy, R. Roy, Al-substituted tobermorite: shows cation exchange, Cem. Concr. Res. 12 (1982) 773–780.
[71] N. Hara, N. Inoue, Thermal behaviour of 11Å tobermorite and its lattice parameters, Cem. Concr. Res. 10 (1980) 53–60.
[72] K. Matsui, J. Kikuma, M. Tsunashima, T. Ishikawa, S.Y. Matsuno, A. Ogawa, M. Sato, In situ time-resolved X-ray diffraction of tobermorite formation in autoclaved aerated concrete: influence of silica source reactivity and Al addition, Cem. Concr. Res. 41 (2011) 510–519.
[73] Y. Going, C.S. Yim, Influence of alumina on Hydrothermal synthsis of 11 Å tobermorite, Korean J. Mater. Res. 15 (2005) 97–105.
[74] S. Diamond, J.L. White, W.L. Dolch, Effects of isomorphous substitution in hydrothermally-synthesized tobermorite, Am. Mineral. 51 (1966) 388–401.
[75] A. Vidmer, G. Sclauzero, A. Pasquarello, Infrared spectra of jennite and tobermorite from first-principles, Cem. Concr. Res. 60 (2014) 11–23.
[76] Y. Yan, S.Y. Yang, G.D. Miron, I.E. Collings, E. L'Hôpital, J. Skibsted, F. Winnefeld, K. Scrivener, B. Lothenbach, Effect of alkali hydroxide on calcium silicate hydrate (C-S-H), Cem. Concr. Res. 151 (2022).
[77] P.F. McMillan, G.H. Wolf, B.T. Poe, Vibrational spectroscopy of silicate liquids and glasses, Chem. Geol. 96 (1992) 351–366.
[78] P. Yu, R.J. Kirkpatrick, B. Poe, P.F. McMillan, X. Cong, Structure of calcium silicate hydrate (C-S-H): near-, mid-, and far-infrared spectroscopy, J. Am. Ceram. Soc. 48 (1999) 742–748.
[79] K. Garbev, P. Stemmermann, L. Black, C. Breen, J. Yarwood, B. Gasharova, Structural features of C-S-H(I) and its carbonation in air-a raman spectroscopic study. Part I: fresh phases, J. Am. Ceram. Soc. 90 (2007) 900–907.
[80] R.J. Kirkpartick, J.L. Yarger, P.F. McMillan, P. Yu, X. Cong, Raman spectroscopy of C-S-H, tobermorite, and jennite, Adv. Cem. Based Mater. 5 (1997) 93–99.
[81] L. Black, C. Breen, J. Yarwood, K. Garbev, P. Stemmermann, B. Gasharova, Structural features of C-S-H(I) and its carbonation in air-a raman spectroscopic study. Part II: carbonated phases, J. Am. Ceram. Soc. 90 (2007) 908–917.
[82] S. Ortaboy, J. Li, G. Geng, R.J. Myers, P.J.M.M. Monteiro, R. Maboudian, C. Carraro, Effects of CO2 and temperature on the structure and chemistry of C-(A-) S-H investigated by raman spectroscopy, RSC Adv. 7 (2017) 48925–48933.
[83] N.Y. Mostafa, A.A. Shaltout, H. Omar, S.A. Abo-El-Enein, Hydrothermal synthesis and characterization of aluminium and sulfate substituted 1.1 nm tobermorites, J. Alloys Compd. 467 (2009) 332–337.

[84] M. Horgnies, J.J. Chen, C. Bouillon, Overview about the use of fourier transform